

SPECTRAL AND POLARIZATION PROPERTIES OF PHOTOSPHERIC EMISSION FROM STRATIFIED JETS

HIROTAKA ITO¹, SHIGEHIRO NAGATAKI¹, JIN MATSUMOTO¹, SHIU-HANG LEE², ALEXEY TOLSTOV^{3,4}, JIRONG MAO^{1,5},
MARIA DAINOTTI¹ AND AKIRA MIZUTA⁶

draft version May 27, 2014,

ABSTRACT

We explore the spectral and polarization properties of photospheric emissions from stratified jets in which multiple components, separated by a sharp velocity shear regions, are distributed in lateral direction. Propagation of thermal photons injected at high optical depth region are calculated until they escape from the photosphere. It is found that presence of the lateral structure within the jet leads to non-thermal feature of the spectra and significant polarization signal in the resulting emission. The deviation from thermal spectra as well as the polarization degree tends to be enhanced as the velocity gradient in the shear region increases. In particular, we show that emissions from multi-component jet can reproduce the typical observed spectra of gamma-ray bursts (GRBs) irrespective to the position of the observer when a velocity shear region is closely spaced in various lateral (θ) positions. The degree of polarization associated in the emission is significant ($> \text{few}\%$) at wide range of observer angles and can be higher than 30%.

Subject headings: gamma ray burst: general — radiation mechanisms: thermal – radiative transfer — scattering —

1. INTRODUCTION

Gamma-ray Bursts (GRBs) are the most luminous phenomena in the Universe. They are transient, intense flashes of gamma-rays occurring at cosmological distances. One of their peculiar features is the rapid variability in their prompt emission light curves. The observed spectrum is highly non-thermal and it is often described by the empirical Band function (Band et al. 1993) that has a smoothly jointed broken power-law shape. The typical break (peak) energy is observed around $\sim 0.1 - 1$ MeV, while the typical photon indices of the low and high energy spectrum are found at $\alpha_{\text{ph}} \sim -1$ and $\beta_{\text{ph}} \sim -2.5$, respectively (Preece et al. 2000; Kaneko et al. 2006, 2008; Nava et al. 2011; Goldstein et al. 2012, 2013).

It is widely accepted that the prompt emission is originated in an ultra-relativistic jet. However, despite the extensive studies in the past decades, exactly how the gamma-rays are produced within the jet remains unclear. Optically thin synchrotron emission originating from internal shocks (Rees & Meszaros 1994; Sari & Piran 1997) has been considered as a standard model for many years. In this model, highly non-thermal features showing a broken power-law and the observed rapid time variability can be achieved naturally. On the other hand, however, it is known that

this model faces several difficulties. Since the internal shocks can only convert the kinetic energy associated with the relative motion within the jet into the gamma-rays, it suffers from poor radiation efficiency (Kobayashi et al. 1997; Lazzati et al. 1999; Guetta et al. 2001; Kino et al. 2004). Additional difficulties are also found in the spectra. A natural mechanism to realize clustering of peak energy at $\sim 0.1 - 1$ MeV is uncertain. Moreover, the synchrotron model predicts the low energy photon index at $\alpha_{\text{ph}} \sim -3/2$ for the electrons in fast cooling regime which conflicts with the observed typical value ($\alpha_{\text{ph}} \sim -1$). Furthermore, non-negligible fraction of the observed bursts shows low energy slope harder than the death line $\alpha_{\text{ph}} = -2/3$ which cannot be produced by usual synchrotron emission (Crider et al. 1997; Preece et al. 1998; Ghirlanda et al. 2003).

Due to these difficulties, photospheric emission model is considered as one of the most promising alternative scenario for the prompt emission mechanism (e.g., Thompson 1994; Eichler & Levinson 2000; Mészáros & Rees 2000; Rees & Mészáros 2005; Lazzati et al. 2009; Pe’er & Ryde 2011; Mizuta et al. 2011; Nagakura et al. 2011; Ruffini et al. 2011; Xu et al. 2012; Bégué et al. 2013; Lundman et al. 2013a; Lazzati et al. 2013). The photospheric emission is an inherent feature of the original fireball model in which the internally trapped photons that accelerate outflow to ultra-relativistic velocity are eventually released at the photosphere (Goodman 1986; Paczynski 1986). Unlike in the internal shock model, high radiation efficiency as well as clustering of the peak energies can be achieved quite naturally. Recent detections of quasi-thermal component in the observed GRB spectra provide a further support that the prompt gamma-rays, at least in part, are originated from the photosphere (e.g., Abdo et al. 2009; Ryde et al. 2010, 2011; Guiriec et al. 2011; Pe’er et al. 2012; Guiriec et al. 2013; Ghirlanda et al. 2013).

On the other hand, since thermal photons are ex-

Electronic address: hirohito.ito@riken.jp

¹ Astrophysical Big Bang Laboratory, RIKEN, Saitama 351-0198, Japan

² Institute of Space and Astronautical Science, Japan Aerospace Exploration Agency, 3-1-1 Yoshinodai, Chuo-ku, Sagami-hara, Kanagawa 252-5210, Japan

³ Kavli IPMU (WPI), University of Tokyo, Chiba 277-8583, Japan

⁴ Institute for Theoretical and Experimental Physics (ITEP), 117218, Moscow, Russia

⁵ Department of Physics, Kyushu University, Fukuoka 812-8581, Japan

⁶ Computational Astrophysics Laboratory, RIKEN, Saitama 351-0198, Japan

pected in a simple photospheric emission model, it is difficult to reproduce the broad non-thermal shape of the observed spectra. Hence, in order to explain the overall spectrum with the photospheric emission alone, an additional mechanism which leads to the broadening in the spectra is required. Several authors claim an efficient dissipation around the photosphere can provide such an effect (e.g., Pe’er et al. 2005, 2006; Giannios 2006; Giannios & Spruit 2007; Giannios 2008; Ioka et al. 2007; Lazzati & Begelman 2010; Beloborodov 2010; Vurm et al. 2011; Asano & Mészáros 2013). The electrons (and positrons) that are heated via dissipative processes such as shocks, magnetic reconnection and proton-neutron collisions can give rise to the non-thermal spectrum close to the observations. However, it seems quite questionable whether dissipative processes can operate efficiently to deposit the copious amount of energy in relativistic electrons (and positrons).

Alternatively, recent studies have shown that broadening of spectrum can also be originated by the effect of geometrical structure of the jet. By considering a gradually decaying profile in the lateral distribution of the bulk Lorentz factor of the jet, Lundman et al. (2013a) found that the typical low energy photon index ($\alpha_{\text{ph}} \sim -1$) can be reproduced by the photospheric emissions. Similar to their approach, but with a larger gradient (velocity shear) in the lateral profile, Ito et al. (2013) (hereafter, Paper I) have shown that, by imposing a sharp gradient on the lateral distribution, fraction of photons that cross the velocity shear region multiple times can gain energy via Fermi-like acceleration mechanism. It is demonstrated that the accelerated photons can give rise to non-thermal tail above the peak energy which reproduces the typical high energy photon index ($\beta_{\text{ph}} \sim -2.5$) of the observed spectra. However, how the structure of the jet is naturally regulated to such a geometry, which can reproduce the observations, remains unclear.

In addition to the spectral features, polarization measurement may be useful to give a further constraint on the prompt emission mechanism. The first detection of linear polarization in the prompt emission was reported by RHESSI from GRB 021206 (Coburn & Boggs 2003). However, independent groups did not confirm the polarization signals using same data (Rutledge & Fox 2004; Wigger et al. 2004). Similarly, INTEGRAL-SPI and -IBIS data showed detection of polarization from GRB 041219, but the results of SPI and IBIS appear inconsistent (Kalemci et al. 2007; McGlynn et al. 2007; Götz et al. 2009). The instrumental systematics are the main obstacles to obtain a convincing result. Recent observation by GAP instrument on board IKAROS realized a detection with quite low systematic uncertainty (Yonetoku et al. 2011). High degree of linear polarization in the prompt emission of GRB 100826A ($27 \pm 11\%$), GRB 110301A ($70 \pm 22\%$), and GRB 110721A ($84^{+16}_{-28}\%$) were reported in the observations (Yonetoku et al. 2011, 2012). It is noted, however, that these results still suffer from low statistics, and $\sim 0\%$ polarization degree cannot be ruled out at $\sim 3\sigma$ confidence level. Future polarimeter missions, such as TSUBAME (Yatsu et al. 2012) and POLAR (Orsi & Polar Collaboration 2011), are awaited to provide more accurate data.

In order to use the polarization measurement as

a probe for the prompt emission mechanism, it is essential to evaluate the polarization signal associated in each emission models. The polarization properties of optically thin models such as synchrotron and inverse Compton emissions have been extensively studied by many authors (e.g., Shaviv & Dar 1995; Lyutikov et al. 2003; Granot 2003; Nakar et al. 2003; Waxman 2003; Eichler & Levinson 2003; Levinson & Eichler 2004; Lazzati et al. 2004; Toma et al. 2009; Lazzati 2006; Zhang & Yan 2011; Mao & Wang 2013). On the other hand, only few studies explored the polarization signals associated with photospheric emissions. First detailed study on this issue was carried out by Beloborodov (2011). He solved a transfer of photons within a steady relativistically expanding opaque outflow, under the assumption of spherical symmetry. Contrary to naive expectation, it is found that significant anisotropy develops in the photon distribution around the photosphere not only in the laboratory frame but also in the fluid comoving frame. Due to the anisotropy, photons released at the photosphere can achieve high level of polarization through last scatterings. However, although the photons released at a local emitting regions can be strongly polarized, superposition of each emission component vanishes the net polarization in the observed emissions for a spherically symmetric outflow. Therefore, to produce a non-negligible polarization signal in the observed emission, the emitting region must show a break of rotational symmetry around the line of sight of the observer within an angle $\sim \Gamma^{-1}$, where Γ is the bulk Lorentz factor of the outflow.

This is indeed shown by Lundman et al. (2014) who studied the polarization properties of the photospheric emission from a jet having lateral structure. The considered geometry is identical to those considered in their previous study (Lundman et al. 2013a) which focused on the spectral features. The bulk Lorentz factor of the jet near the center is approximately constant up to a certain angular width and an approximately power-law decaying profile is imposed at a larger angle $\Gamma \propto \theta^{-p}$. By solving the photon transfer, they found that a significant polarization signal can be accompanied in photospheric emissions originating from a jet with such a geometry. Particularly, they showed that a narrow jet that has a steep Lorentz factor gradient at the outer region can produce a quite high polarization degree up to $\sim 40\%$. It is noted, however, that high polarization degrees $\gtrsim 10\%$ can be detected only by an observer that has line of sight, hereafter called LOS, aligned in the outer regions. The emissions viewed by such an off-axis observer are much dimmer than those observed by an on-axis observer. Moreover, while they showed that a highly non-thermal broken-power law shape of the spectra is an inherent feature of the emissions, the spectral slopes have a strong dependence on the observer position particularly at high energies and may deviate largely from the typically observed ones at a large fraction of observers.

As discussed in Paper I, the strong dependence of the spectral slopes on the observers can be reduced when a velocity shear regions are present at various lateral position of the jet. For example, if a velocity shear region is distributed within the entire jet, non-thermal photons originated at the velocity shear regions due to photon acceleration can be prominent for all observers. Indeed,

such a rich internal structure within the jet is inferred in a recent numerical simulations (Matsumoto & Masada 2013a,b). In these simulations, they explored the evolution of the transverse structure of the relativistic jet during its propagation in a dense medium. Their results indicated that hydrodynamical instabilities such as Rayleigh-Taylor and Richtmyer-Meshkov instabilities produce small scale filamentary structures that have sharp interface to distribute in entire jet regions.

Motivated by these backgrounds, we explore the photospheric emissions from a stratified jet that has velocity shear regions at various angular (θ) positions in the present study. Main purpose of our study is to further investigate the effect of jet geometry on the spectral and polarization properties. Analogously to Paper I, here it is assumed that components with uniform fluid properties are separated by a sharp boundary transition layers. We show, in particular, that, when a velocity shear region is closely spaced within an angular scale $\sim 2\Gamma^{-1}$, typical Band spectra can be reproduced irrespective to the observer position. We also show that a high polarization degrees $\gtrsim 10\%$ can be detected not only by the observers viewing dim emissions, but also those viewing brightest emissions.

The paper is organized as follows. In §2, we describe our model and numerical procedures used in our calculations. We present the main results in §3. Discussions are given in §4. The summary of our main findings is given in §5.

2. MODEL AND METHODS

In the present study, we evaluate the photospheric emissions from an ultra-relativistic jet with a half-opening angle θ_j in which a stratified structure is present in the lateral (θ) direction. We consider two types for the stratification: (I) two-component (spine-sheath) jet in which fast spine jet is embedded in a slower sheath outflow and (II) multi-component jet which is composed of multiple outflow layer of finite lateral width. The schematic picture of the two models are shown in Figs. 1 and 2.

In both models, we assume a sharp transition layer between each component that has lateral width $d\theta_B$. As for the two-component jet model, the spine region defined as a region of conical outflow with a half-opening angle $\theta_0 - d\theta_B/2$, while the sheath is a region that surrounds the spine and has an angular extension of $\theta_0 + d\theta_B/2 \leq \theta \leq \theta_j$. In the multi-component jet model, two components having fixed widths of $d\theta_0 - d\theta_B$ (Component 0, hereafter C0) and $d\theta_1 - d\theta_B$ (Component 1, hereafter C1) alternately appear in the transverse direction. While the first component located at the center is a conical outflow with a half-opening angle $(d\theta_0 - d\theta_B)/2$, other components have sheath structures which have the same central axis. The repeated pattern of this transverse structure continues until the total angular extension reaches the half opening angle of the jet, θ_j . As described below, the properties of the spine (sheath) in the two-component jet model are determined in the same manner as C0 (C1) in the multi-component jet model. Hereafter, the quantities corresponding to the spine (C0) and sheath (C1) regions are denoted by subscripts 0 and 1, respectively. The quantities without the subscript refer to all regions including the boundary transition layers.

It is noted that the two-component jet model is introduced to clarify the effects of sharp velocity gradients on the resulting spectra and the polarization. Main difference between the present paper and Paper I is that here we include and quantify the polarization signal. On the other hand, multi-component jet model is introduced in order to explicitly show that the existence of sharp velocity gradient regions within an angular scale $\sim 2\Gamma^{-1}$ is essential to reproduce the typical observed spectra of GRBs and to quantify the polarizations associated with these emissions. Although the assumed geometry of the employed models is somewhat artificial, it is stressed that similar results are expected if sharp velocity shear regions are present in the transverse structure of the jet and are closely distributed within a small angular scale $\sim 2\Gamma^{-1}$. Such a rich internal structure is indeed inferred from the recent numerical simulations (e.g., Matsumoto & Masada 2013a,b). We will mention on this issue later in §3.3 and §4.1.

2.1. Fluid Properties of Stratified Jet

We consider a steady radially expanding axisymmetric outflow, and the radial profile of the fluid properties are described by the standard adiabatic fireball model (e.g., Piran 2004; Mészáros 2006, and also see Paper I for a brief review) which can be determined uniquely by the three independent parameters: the initial radius, r_i , the kinetic luminosity, L , and the dimensionless entropy (or, equivalently the terminal Lorentz factor) $\eta \equiv L/\dot{M}c^2$, where \dot{M} and c are the mass outflow rate and the speed of light, respectively. In the present study, we only consider the case in which the photosphere, r_{ph} , the radius where the fireball becomes optically thin (see Eq. (4)), is located above the saturation radius, $r_s = \eta r_i$, the radius where the bulk acceleration of the fireball ceases. Hence, the three parameters in all regions satisfy $\eta < \eta_c = (\sigma_T L / 8\pi r_i m_p c^3)^{1/4}$, where σ_T and m_p are the Thomson cross section and proton rest mass, respectively.

Given the three parameters, the radial evolution of the bulk Lorentz factor and the electron number density is determined by

$$\Gamma(r) = \begin{cases} \frac{r}{r_i} & \text{for } r \leq r_s, \\ \eta & \text{for } r > r_s, \end{cases} \quad (1)$$

and

$$n_e(r) = \frac{\dot{M}}{4\pi r^2 m_p \Gamma \beta c} = \frac{L}{4\pi r^2 m_p \eta \Gamma \beta c^3}, \quad (2)$$

where β is the velocity of the flow normalized by the speed of light. The electron number density decreases with radius as $n_e \propto r^{-3}$ below the saturation radius ($r \leq r_s$) and as $n_e \propto r^{-2}$ at larger radii ($r > r_s$). Given the electron number density and bulk Lorentz factor of the flow, the optical depth to Thomson scatterings for the photons propagating in the *radial* direction to reach infinity can be evaluated as

$$\begin{aligned} \tau(r) &= \int_r^\infty \sigma_T n_e(r') \Gamma(r') (1 - \beta(r')) dr' \\ &\simeq \begin{cases} \frac{r_{ph}}{r} \left[1 + \frac{1}{3} \left\{ \left(\frac{r_s}{r} \right)^2 - \left(\frac{r}{r_s} \right)^2 \right\} \right] & \text{for } r \leq r_s, \\ \frac{r_{ph}}{r} & \text{for } r > r_s, \end{cases} \quad (3) \end{aligned}$$

$$r_{\text{ph}} = \frac{\sigma_T L}{8\pi\eta^3 m_p c^3}, \quad (4)$$

where we have assumed $\Gamma \gg 1$ (Abramowicz et al. 1991). Here, r_{ph} is the radius where the optical depth becomes unity ($\tau = 1$).

2.1.1. Transverse structure

Here, we describe how the transverse structure of the jet is determined. The transverse structure plays an essential role on the spectral and polarization properties of the resulting emissions.

In all regions, We impose the same value of the initial radius, r_i . Different values are imposed for the dimensionless entropy of the spine (C0), η_0 and sheath (C1) region, η_1 . In all cases we assume $\eta_0 > \eta_1$. As explained later, due to this difference, strong velocity shear region appears within the jet. The transverse (θ) distribution of the dimensionless entropy at the boundary transition layer is determined by simply imposing a linear interpolation from the surrounding two regions which can be written as

$$\eta(\theta) = \frac{(\theta - \theta_B + d\theta_B/2)\eta_{\text{ii}} + (\theta_B + d\theta_B/2 - \theta)\eta_{\text{i}}}{d\theta_B}, \quad (5)$$

where θ_B is the angle at midpoint of the transition layer. The subscripts i and ii correspond to 0 (1) and 1 (0), respectively, when $\theta_B - d\theta_B/2$ and $\theta_B + d\theta_B/2$ are the angle at the edge of component with dimensionless entropy of η_0 (η_1) and η_1 (η_0), respectively. Fig. 3 shows the overall transverse distribution of the dimensionless entropy (terminal Lorentz factor).

In determining the kinetic luminosities, we assume that the mass outflow rate is equal in all regions ($L/\eta = \text{constant}$). Hence, kinetic luminosity of the spine (C0) is larger by a factor of η_0/η_1 , than that of the sheath (C1).

Due to the difference in the imposed parameters, the saturation radius of the spine (C0) $r_{s0} = \eta_0 r_i$ is located above that of the sheath (C1) $r_{s1} = \eta_1 r_i$. Since $\eta(\theta)$ is determined by the linear interpolation from the surrounded two regions, the saturation radius at the layer is also a linear interpolation from r_{s0} and r_{s1} . As a result, the bulk Lorentz factor in all regions has equal values ($\Gamma(r) = r/r_i$) up to $r = r_{s1}$, and, at a larger radii, ($r > r_{s1}$), velocity shear begins to develop at the boundary layer until $r = r_{s0}$. Thereafter, the velocity difference is fully developed and all regions are in the coasting phase with a terminal Lorentz factor (see Fig. 3, for the resulting distribution).

Regarding the transverse distribution of the photosphere, the photospheric radius in the spine (C0) region, $r_{\text{ph}0}$, is smaller than in the sheath (C1) region, $r_{\text{ph}1}$, by a factor of $(\eta_0/\eta_1)^2$ (see equation (4)). The photospheric radius in the boundary transition layer also scales as $\propto (\eta_0/\eta(\theta))^2$ and continuously connects the surrounding two regions.

2.2. Photon Transfer

Having determined the background fluid properties (Γ and n_e), we evaluate the resultant photospheric emission by solving the propagation of photons. The photon

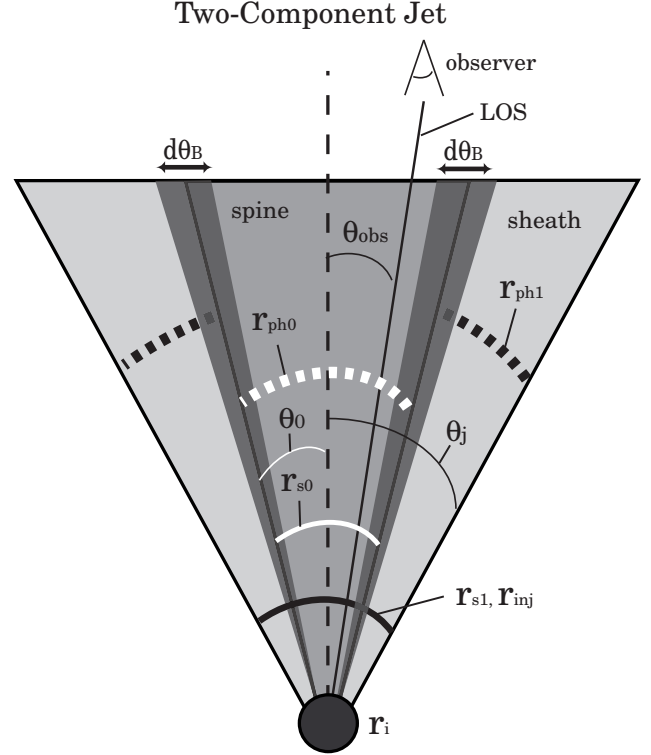


FIG. 1.— Schematic picture of our two-component (spine-sheath) jet model. A fast spine jet ($\theta \leq \theta_0 - d\theta_B/2$) is embedded in a slower sheath outflow ($\theta_0 + \theta_B/2 \leq \theta \leq \theta_j$). The spine and sheath start to accelerate at radius r_i . The acceleration continues up to r_{s0} and r_{s1} in the spine and sheath region, respectively. Since the dimensionless entropy of the spine η_0 is larger than that of the sheath η_1 , the saturation radius and the terminal Lorentz factor of the spine ($r_{s0} = \eta_0 r_i$ and $\Gamma_0 = \eta_0$) are larger than those of the sheath ($r_{s1} = \eta_1 r_i$ and $\Gamma_1 = \eta_1$). The photospheric radius of the spine $r_{\text{ph}0}$ is smaller than that of the sheath $r_{\text{ph}1}$, where the photospheric radius is defined by Eq. (4). There is a transition layer with an angular width $d\theta_B$ between the spine and sheath ($\theta_0 - \theta_B/2 \leq \theta \leq \theta_0 + \theta_B/2$). The dimensionless entropy and kinetic luminosity in this region are determined by the interpolations from the two regions. In our calculation, thermal photons are injected at the saturation radius of the sheath $r_{\text{inj}} = r_{s1}$, and their transfer is solved up to the radius at which the optical depth is much lower than unity.

transfer is evaluated by performing a three-dimensional test particle Monte-Carlo simulation. In GRB jets, opacity of photons is strongly dominated by the scatterings with electrons (Pe'er & Ryde 2011; Beloborodov 2011). Therefore, we neglect the absorption process and only consider the scattering process by the electrons. Furthermore, for simplicity, we do not take into account the thermal motion of the electrons in evaluating the scattering. Hence, the rest frame of the fluid is equivalent to that of the electrons.

The Monte-Carlo code used in the present study is basically the same as the ones used in Paper I. We directly track the path of the individual photon packets that undergoes multiple-scatterings with the electrons in the jets. The main difference from the previous study is that we evaluate the polarization state of the photon packet, and include its effect on the electron scattering. Each photon packet carries a specified four momentum (or, equivalently the frequency, ν , and the propagation direction \mathbf{n}). In addition, the Stokes parameters $S = (I, Q, U, V)$ which determine the polarization

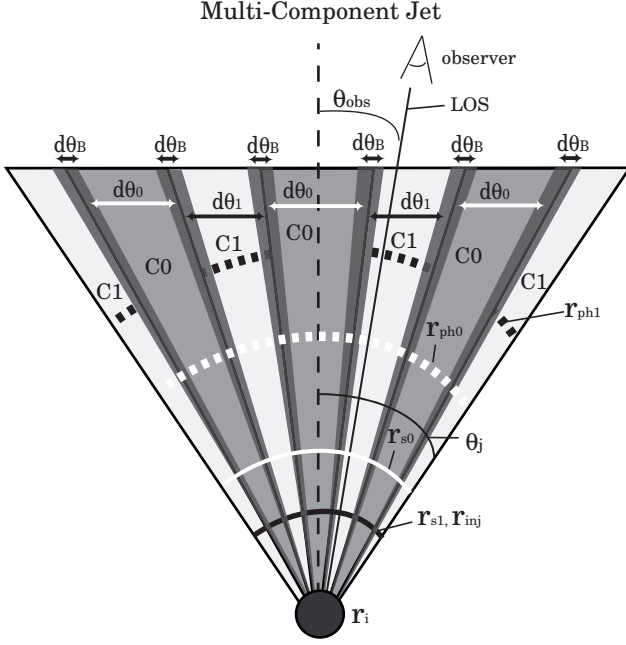


FIG. 2.— Schematic picture of our multi-component jet model. Two components having fixed widths of $d\theta_0 - d\theta_B$ (C0) and $d\theta_1 - d\theta_B$ (C1) alternately appear in the transverse direction within the jet with half opening angle θ_j . There are transition layers with an angular width $d\theta_B$ between the two components. The radial profile of C0 and C1 as well as the transition layer are determined in the same way as in the two-component jet model.

state are also carried. The evolution of these quantities via electron scattering is calculated self-consistently by properly taking into account the effect of the polarization state on the scattering process (for detail, see Appendix).

The parameter I corresponds to the intensity which we set to be equal to the total energy carried by the packet. The parameters Q and U characterize the linear polarizations with respect to arbitrary orthogonal $x - y$ axes in the plane of the polarization (plane that is perpendicular to the photon propagation direction) and to a set of axes oriented at 45° to the anti-clockwise direction of the previous one, respectively. The parameter V characterizes the circular polarization. However, V is not relevant in our calculations since we assume that the initially injected photons are unpolarized ($Q = U = V = 0$) and that spin of the electrons are isotropically distributed. Under these assumptions, scatterings only lead to the changes in the linear polarizations and $V = 0$ is always conserved.

The x - and y -axes used to define the Stokes parameters are aligned in a plane formed by a direction vector of photon \mathbf{n} and the jet axis and to a direction perpendicular to the plane, respectively. We illustrate the coordinates and polarization plane mentioned above in Fig. 4. The photons propagating in the same direction have the same coordinate system, because even though the direction of the axes temporarily changes during the computation of the scattering effect on the polarization state (Appendix), after the calculation, the Stokes parameters are always redefined in the above coordinate system.

Initially, the photons are injected within the jet at the surface of a fixed radius where the velocity shear begins to develop $r_{\text{inj}} = r_{s1}$. For the cases considered in this study, r_{inj} is always located far below the photosphere

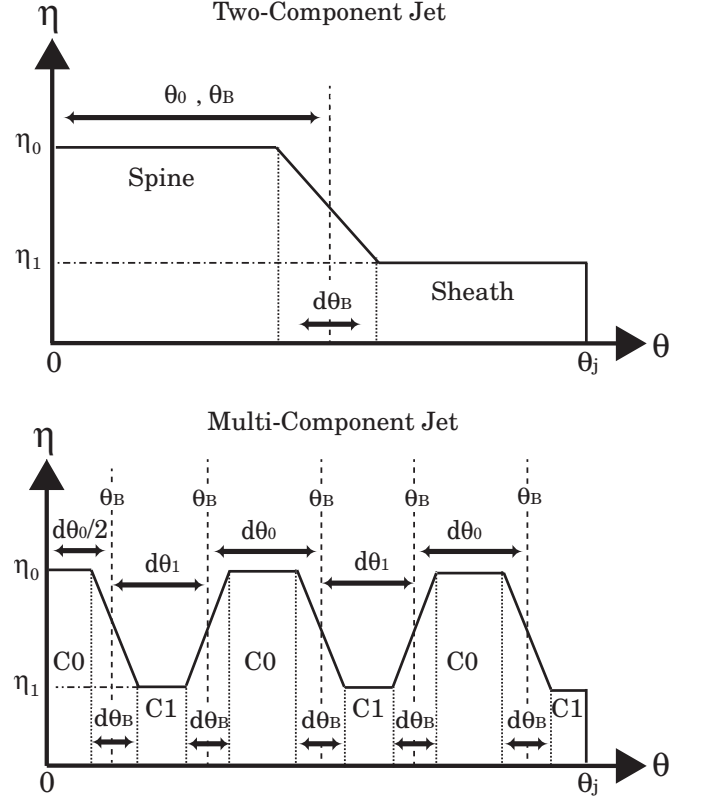


FIG. 3.— The transverse (θ) distribution of the dimensionless entropy (terminal Lorentz factor) η . The top and bottom panels correspond to the two-component and multi-component jet model, respectively.

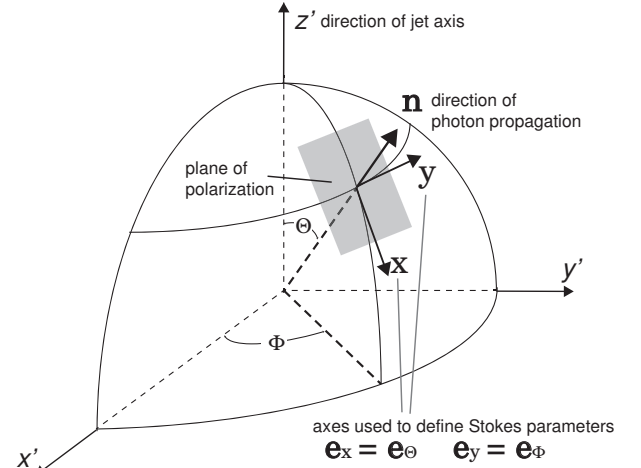


FIG. 4.— The plane of polarization and coordinate systems that are used to define the Stokes parameters. The vector \mathbf{n} shows the direction of the photon propagation. The plane of polarization is defined as a plane normal to \mathbf{n} . By introducing a Cartesian coordinate system that has its z -axis aligned to the direction of the jet axis (shown by x', y' and z'), and the corresponding spherical coordinate system, the propagation direction of a photon can be defined by two angles: Θ , the angle between vector \mathbf{n} and the z' -axis, and Φ , the angle between the projected vector of \mathbf{n} in the $x'-y'$ plane and the x' -axis. The directions of the x - and y -axes that are used to define the Stokes parameters are aligned to the direction of two basic vectors of the spherical coordinate system \mathbf{e}_Θ and \mathbf{e}_Φ , respectively.

($\tau(r_{\text{inj}}) \gg 1$). Therefore, a tight coupling between the

photons and matter is ensured. For this reason, we can safely assume that the photons have an isotropic distribution with energy distribution given by a Planck distribution in the comoving frame and these photons are unpolarized.

According to the fireball model, the radial evolution of the comoving temperature is given by

$$T'(r) = \begin{cases} \left(\frac{L}{4\pi r_i^2 ca}\right)^{1/4} \left(\frac{r}{r_i}\right)^{-1} & \text{for } r \leq r_s, \\ \left(\frac{L}{4\pi r_i^2 ca}\right)^{1/4} \left(\frac{r_s}{r_i}\right)^{-1} \left(\frac{r}{r_s}\right)^{-2/3} & \text{for } r > r_s, \end{cases} \quad (6)$$

where a is the radiation constant. Hence, we adopt the temperature at the corresponding radius given by above equation $T'_{\text{inj}} = T'(r_{\text{inj}})$ for the comoving temperature of the injected photons. Due to this relativistic effect, the radiation intensity of the blackbody emission in a relativistically expanding flow is given by

$$I_{\nu, \text{inj}}(\nu) = \mathcal{D}(\Gamma_{\text{inj}}, \theta_v)^3 B_\nu(T'_{\text{inj}}, \nu/\mathcal{D}(\Gamma_{\text{inj}}, \theta_v)), \quad (7)$$

where $\Gamma_{\text{inj}} = \Gamma(r_{\text{inj}})$ is the bulk Lorentz factor of the flow at $r = r_{\text{inj}}$ determined from equation (1). Here, $B_\nu(T', \nu) = 2h\nu^3 c^{-2} [\exp(h\nu/k_B T') - 1]^{-1}$ is the Planck function, where h and k_B are the Planck constant and the Boltzmann constant, respectively, and $\mathcal{D}(\Gamma, \theta_v) = [\Gamma(1 - \beta \cos \theta_v)]^{-1}$ is the Doppler factor, where θ_v is the angle between the photon propagation direction and the fluid velocity direction (radial direction). In our calculation, the initial propagation direction and frequency of the injected photons are drawn from a source of photons given by the above equation. Initially, the total energy of the packet I is set to be equal among all the photon packets. As mentioned above, the remaining Stokes parameters are set to be 0 ($Q = U = V = 0$), since the photons far below the photosphere are expected to be unpolarized.

After the the photon packet is injected, we follow the track of the individual photons using the Monte-Carlo technique. Initially, the code determines the distance for the photons to travel before the scattering by drawing the corresponding optical depth $\delta\tau$. The probability for the selected optical depth to be in the range of $[\delta\tau, \delta\tau + d\tau]$ is given as $\exp(-\delta\tau)d\tau$. Then, from the given optical depth $\delta\tau$, the distance l to the scattering event is determined from the integration along the straight path of photons which can be expressed as

$$\delta\tau = \int_0^l n_e \Gamma(1 - \beta \cos \theta_v) \sigma_{\text{sc}} dl. \quad (8)$$

Here, σ_{sc} is the total cross section for the electron scattering and is given as

$$\sigma_{\text{sc}} = \begin{cases} \sigma_{\text{T}} & \text{for } h\nu_{\text{cmf}} \leq 100 \text{ keV}, \\ \sigma_{\text{KN}} & \text{for } h\nu_{\text{cmf}} > 100 \text{ keV}, \end{cases} \quad (9)$$

in our code, where σ_{KN} is the total cross section for Compton scattering, and ν_{cmf} is the frequency of the photon in electron (fluid) comoving frame. The frequency ν_{cmf} is evaluated by performing a Lorentz transformation using local fluid velocity.

Given the distance l from the above equation, we update the position of the photons to the scattering position by shifting them from the initial position with the

given distance along the direction of photon propagation. Note that, unlike the case of Eq. (3), the optical depth calculated by Eq. (8) is not limited to photons propagating in the radial direction. The path of integration is along the straight path of photons which can be in an arbitrary direction. For a given value of $\delta\tau$, the distance l strongly depends on the propagation direction of the photons in the case of a relativistic flow ($\Gamma \gg 1$). This is because the mean free path of photons $l_{\text{mfp}} = [n_e \Gamma(1 - \beta \cos \theta_v) \sigma_{\text{sc}}]^{-1}$ is quite sensitive to the photon propagation direction, since the factor $\Gamma(1 - \beta \cos \theta_v)$ varies largely from $\sim (2\Gamma)^{-1}$ (for $\cos \theta_v = -1$) up to $\sim 2\Gamma$ (for $\cos \theta_v = 1$) depending on the value of θ_v . Hence, a photon tends to travel a larger distance in the fluid velocity (radial) direction, since the mean free path of the photon tends to be larger.

Given the position for the scattering from the above procedure, the four-momentum (the frequency and propagation direction) and the Stokes parameters of a photon packet after the scattering is determined based on the differential cross section for electron scattering. Here we give the brief overview of our calculation (for detail see Appendix). In our code, the scattering process is evaluated in the rest frame of the fluid. First, the four-momentum of the photon before the scattering is Lorentz transformed from laboratory frame to the fluid rest frame. For the photons that satisfy $h\nu_{\text{cmf}} \leq 100 \text{ keV}$, the Klein-Nishina effect is neglected, while the full Klein-Nishina cross section is used at higher energies ($h\nu_{\text{cmf}} > 100 \text{ keV}$). The effect of polarization on the differential cross sections is self-consistently included in both regimes. The scattering angle or equivalently the propagation direction of the scattered photon in the fluid rest frame is drawn from the differential cross sections. Once the scattering angle is determined, we update the four-momentum and the Stokes parameters to that of the scattered photons. While the frequency and total energy carried by a photon packet (ν and I) are conserved after the scattering (elastic scattering) for $h\nu_{\text{cmf}} \leq 100 \text{ keV}$, energy loss due to the recoil effect is taken into account for $h\nu_{\text{cmf}} > 100 \text{ keV}$. Also, the Stokes parameter of the scattered photon packet is obtained from the incident one by properly taking into account the Klein-Nishina effect for $h\nu_{\text{cmf}} > 100 \text{ keV}$, while the effect is neglected for $h\nu_{\text{cmf}} \leq 100 \text{ keV}$. Then the four-momentum of the scattered photon is transformed back into laboratory frame.

The above procedure is repeated until all the injected photons reach the outer boundary or inner boundary of the calculation. The outer boundary in the radial direction is set at a radius $r_{\text{out}} = 2000r_{\text{ph0}}$ where the photons can be safely considered to have escaped since the optical depth in all region is much smaller than unity ($\tau(r_{\text{out}}) \ll 1$). The outer boundary in the transverse (θ) direction is set at the edge of the jet $\theta_{\text{out}} = \theta_j$. As for the inner boundary, we adopt a radius slightly below the injection radius $r_{\text{in}} = 0.5r_{\text{inj}}$. For photons which have reached the outer boundaries, we assume that they escape freely to $r = \infty$ without being scattered or absorbed. On the other hand, we assume that the photons are simply absorbed in the inner boundary. It is noted, however, that the fraction of absorbed photons is negligible, since most of the photons in ultra-relativistic outflows are strongly collimated due to the relativistic beaming effect and essentially streamed outward (e.g.,

Pe'er & Ryde 2011; Beloborodov 2011).

2.3. Evaluation of the Observed Spectrum and Polarization

After the calculations, the spectra and the polarization of the emission are evaluated from the photon packets which have reached the outer boundaries. Due to the relativistic beaming effect, the emission depends strongly on the angle between the direction to the observer and the jet axis, θ_{obs} (see Figs. 1 and 2). In the present study, we evaluate the observed spectrum and polarization by recording all escaped packets that are propagating within a cone of half-opening angle $(4\eta_0)^{-1}$ around the LOS of a given observer. The employed width of the cone is small enough to regard that the emission is uniform within the cone. In evaluating the spectra, for a given frequency bins, we sum up the total energy carried by the photon packets I within the cone, and convert to the isotropic equivalent luminosity by multiplying it with a factor $4\pi/d\Omega$, where $d\Omega$ is the solid angle of the cone. In the same way, all Stokes parameters (I , Q , U and V) are summed up in the given frequency bins and solid angles to evaluate the corresponding Stokes parameters of the total emissions. The polarization signal of the observed emission is evaluated from these parameters.

It is noted that the results of our calculation are insensitive to the assumed position of the injection radius as long as $r_{\text{inj}} \leq r_{\text{s1}}$ is satisfied, and the observer angle, θ_{obs} , (angle between the LOS and the jet axis) is limited in the range $\theta_{\text{obs}} \lesssim \theta_j - \Gamma^{-1}$. The former condition comes from the fact that, at a radius far below the photosphere ($\tau(r) \gg 1$), the photon distribution does not deviate from the isotropic Planck distribution and remains unpolarized, if velocity shear is not present (see next section), and its temperature evolution is well described by Eq. (6). The latter condition is required, since the photons near the jet edge escape during their propagation. Larger fraction of photons escape when smaller injection radius is assumed. Hence, the resulting spectra and the polarization have dependence on the given injection radius. However, it is noted that, while the dependence is strong for an observer that have LOS located outside the lateral jet boundary ($\theta_{\text{obs}} > \theta_j$), weak dependence is found at smaller observer angle, and quantitatively similar results are obtained when the injection radius is set far below the photosphere. Therefore, in the present study, we focus on the observers that have LOS aligned within the jet region $\theta_{\text{obs}} \leq \theta_j$ and do not consider the cases for larger observer angles.

As mentioned above, circular polarization is absent and only linear polarization is found in our calculation, since the circular polarization parameter always satisfies $V = 0$. Also, due to the imposed axisymmetry and the employed coordinate system for the Stokes parameters (Fig. 4), the parameter U vanishes after summing up (see e.g., Chandrasekhar 1960; Beloborodov 2011). We have checked this in our calculation and indeed found that the parameter U converges to 0 as the number of photon packets increases. The number of the packets employed in our calculation is sufficiently large to consider that this convergence is achieved. Therefore, the non-zero Stokes parameters are I and Q . As a result, the polarization state of the observed emissions are characterized by the two parameters and the degree of polarization given by

$|Q|/I$. When Q is positive (negative), the electric vector of the polarized emission is aligned to $x(y)$ -axis shown in Fig. 4. Hence, the positive Q corresponds to the case for electric vector aligned in the plane formed by photon propagation direction (LOS) and jet axis, while the negative Q corresponds to the case for that aligned to perpendicular to the plane.

Finally, let us comment on the expected polarization signature in the stratified jet. As mentioned above, electron scattering of an unpolarized photon packet results in a linearly polarized outgoing photon packet. In Thomson regime (majority of scatterings in our calculation occurs in this regime), the degree of polarization depends only on the scattering angle θ_{sc} , and 100% polarization is found when $\theta_{\text{sc}} = 90^\circ$. The electric vector of the scattered photon is perpendicular to the plane in formed by the incoming and outgoing photon directions. Hence, emissions from scattering dominated photosphere have a potential to produce large linear polarization degree.

In order to produce non-zero polarization degree in the net polarization of the emitted photons, photon distribution in the comoving frame must be anisotropic near the photosphere (last scattering surface). This is because isotropically distributed photons do not have preferential direction in the scattered photon field, and all the polarization signal produced by the scattering will vanish as a whole. As shown by Beloborodov (2011), anisotropy is naturally produced in a scattering dominated photosphere of relativistically expanding fireball. In a relativistically expanding outflow, mean free path of the photons has large dependence on the propagation direction. The photons that propagate along the fluid velocity (radial direction) have larger mean free path than those propagating in other direction. This effect leads the photons to become concentrated in a radial direction. On the other hand, scattering tends to reduce the anisotropy by re-randomizing the propagation direction of the photons. When the photons are far below the photosphere, mean free path of the photons is small enough to keep the photons to be isotropic due to the latter effect. However, when the photons reach near the photosphere the former effect can be significant to produce the anisotropy in the comoving frame, since the mean free path becomes large. As a result, substantial degree of polarization ($\gtrsim 10\%$) can be found in the photons released at the last scattering surface. The strongest polarization is found for the photons that propagate in the direction at an angle $\sim 90^\circ$ respect to the radial direction in the comoving frame. This is due to the fact, that the photons are mainly composed of population that have scattered in an angle close to 90° , since the photon intensity is concentrated in the radial direction. Hence, in an laboratory frame, the strongest polarization is found in the photons that are emitted (last scattered) at an angle $\sim \Gamma^{-1}$ respect to the radial direction. The electric vector of the linearly polarized photons is aligned to the direction perpendicular to the plane formed by photon propagation direction and radial direction.

It is noted, however, that producing a polarized emissions at a local emitting region is not a sufficient condition for a polarization signal to be present in the detected emissions. This is because the polarization can vanish when contributions from the total emitting regions are summed up. In an outflow that is expanding in a radial

direction with a bulk Lorentz factor Γ , most of the detectable emissions come from the regions within the cone of half opening angle $\sim \Gamma^{-1}$ around the LOS of a given observer. Hence, if the emission region is spatially axisymmetric within the cone, the emitted polarized signatures cancel out as a whole. Therefore, in addition, break of the axisymmetry in the emission region around the LOS within an angle $\sim \Gamma^{-1}$ is also a required condition for producing the detectable polarization (Beloborodov 2011; Lundman et al. 2014).

The stratified jet considered in the present study satisfies the above two conditions, and therefore, substantial degree of polarization can be present in the observed emissions.

3. RESULTS

In this section, we show the obtained photon spectra and polarization based on the model described in the previous section. We inject $N = 3 \times 10^8$ photon packets in each calculation. Note that the setup of the calculation for the uniform jet (§3.1) and two-component jet model (§3.2) are basically identical to the ones adopted in Paper I. As mentioned in the previous section, Main difference is that here we calculate the polarization state of the photon and its effect on the scattering (this was neglected in the previous study).⁷

3.1. Uniform (Non-Stratified) Jet

Before considering a stratified jet, we first present results for a one-component uniform jet that does not have structures in the θ direction ($\theta_0 = \theta_j = 1^\circ$). The isotropic equivalent kinetic luminosity, the dimensionless entropy (terminal Lorentz factor) and the initial radius of the fireball are set to be $L_0 = 10^{53} \text{ erg s}^{-1}$, $\eta_0 = 400$ and $r_i = 10^8 \text{ cm}$, respectively. Unpolarized photon packets ($Q = U = V = 0$) are injected at a radius $r_{\text{inj}} = 4 \times 10^{10} \eta_{0,400} r_{i,8} \text{ cm}$ with intensity given by a blackbody of comoving temperature $k_B T'_{\text{inj}} = 1.7 r_{i,8}^{-1/2} \eta_{0,400}^{-1} L_{0,53}^{1/4} \text{ keV}$ (see §2 for detail), where $\eta_{0,400} = \eta_0/400$, $L_{0,53} = L_0/10^{53} \text{ erg s}^{-1}$ and $r_{i,8} = r_i/10^8 \text{ cm}$.

In Fig. 5, we display the obtained numerical results. The left panel shows the spectra for various observer angles θ_{obs} . The obtained spectra have thermal shape due to the absence of sharp structures inside the jet. For an observer located at $\theta_{\text{obs}} \lesssim \theta_j - \eta_0^{-1} \sim 0.86^\circ$, the results do not vary from those obtained in the case for spherical outflow, since the effect of the lateral jet boundary is not significant for the photons located at $\theta \sim \theta_j - \eta_0^{-1} \sim 0.86^\circ$ due to the relativistic beaming effect. Hence, observed spectra are almost identical at this range of the observer angle. The peak energy and luminosity can be estimated as $E_p \sim 800 r_{i,8}^{1/6} \eta_{400}^{8/3} L_{53}^{-5/12} \text{ keV}$ and $L_p \sim 10^{52} r_{i,8}^{2/3} \eta_{400}^{8/3} L_{53}^{1/3} \text{ erg s}^{-1}$, respectively (see Paper I for detail). At a larger observer angle ($\theta_{\text{obs}} \gtrsim \theta_j - \eta_0^{-1} \sim 0.86^\circ$), while the shapes of the spectra remain nearly unchanged, instead the luminosity decreases as the observer angle increases. This is simply because a fraction of the cone of half opening angle $\sim \eta_0^{-1}$ around

LOS falls out the lateral jet boundary ($\theta > \theta_j$). The obtained spectra are broader than the Planck function. Somewhat softening is seen in below the peak energy, resulting in the spectra $\nu L_\nu \propto \nu^2$, in contrast with the Planck one $\nu L_\nu \propto \nu^3$.⁸ This is due the contribution of regions off-aligned from the LOS that have lower thermal peak energies due to the smaller Doppler factor.

The right panel of Fig. 5 shows the dependence of polarization signal Q/I as a function of the observer angle. The thick black solid line shows the result obtained by summing up the total photons, while the red, blue and green solid lines correspond to the cases for the photons in the limited frequency bins of 10 keV – 100 keV, 100 keV – 1 MeV and 1 MeV – 10 MeV, respectively. As mentioned in §2.3, break of axisymmetry in the emission region around the LOS within an angle $\sim \eta_0^{-1}$ is required to produce non-zero polarization degree. In the case of the uniform jet, the origin of the asymmetry in the emission region is solely due to the presence of the jet edge. Therefore, the polarization degree equals zero when the observer angle is well below $\theta_j - \eta_0^{-1} \sim 0.86^\circ$, since the effect of the jet edge is negligible. Although small ($|Q|/I \lesssim 3\%$), non-zero polarization degree is found at a larger observer angle. Regarding the dependence of Q/I on the observer angle, it increases with the observer angle, and then drops to zero or negative at $\theta_{\text{obs}} \sim \theta_j$.

The behaviour of the polarization at observer angles near to the jet edge can be explained as follows: as mentioned in §2.3, when the observer angle is close to but below the jet opening angle $\theta_{\text{obs}} \lesssim \theta_j$, a fraction of the cone of half opening angle $\sim \eta_0^{-1}$ around LOS falls out the lateral jet boundary ($\theta > \theta_j$). First, as the observer angle increases, the emission regions that produce negative Q photon fluxes (electric vector of polarization perpendicular to the plane formed by the LOS and the jet axis) are cut away. Therefore, the observed net polarization have a positive Q . As the observer angle becomes much closer to the jet edge, also the regions emitting photons having positive Q begins to be cut away. Hence, it leads to the decrease in Q/I . The photon fluxes with positive and negative Q nearly balance at $\theta_{\text{obs}} \sim \theta_j$ to produce unpolarized signature.

Regarding the dependence on the frequency, the increase and decrease in Q/I tend to appear at smaller θ_{obs} for low energy photons (10 keV – 100 keV) than those for higher energy photons. This is due to the fact that the photon with energies far below the peak is produced mainly at the regions more off-aligned from the LOS than those with higher energies. The contribution of off-aligned component becomes important at low energies because the Doppler factor is smaller.

3.2. Two-component Jet

3.2.1. Infinitesimal boundary width $d\theta_B = 0$

Here we show the results for a two-component stratified jet model in which the width of the boundary transition layer is infinitesimal ($d\theta_B = 0$). We consider two cases where the imposed fireball parameters in the

⁷ It is also noted that, since the effect of the polarization on the overall track of the photon propagation is not significant, the obtained spectra are almost identical to those obtained in the previous study.

⁸ In Paper I, although the obtained spectra were identical, the evaluation of low-energy spectral slope was not accurate and indicated in the text as $\nu L_\nu \propto \nu^{2.4}$. It is noted that the estimation in the present paper ($\nu L_\nu \propto \nu^2$) is more accurate and is in agreement with other studies (e.g., Bégué et al. 2013).

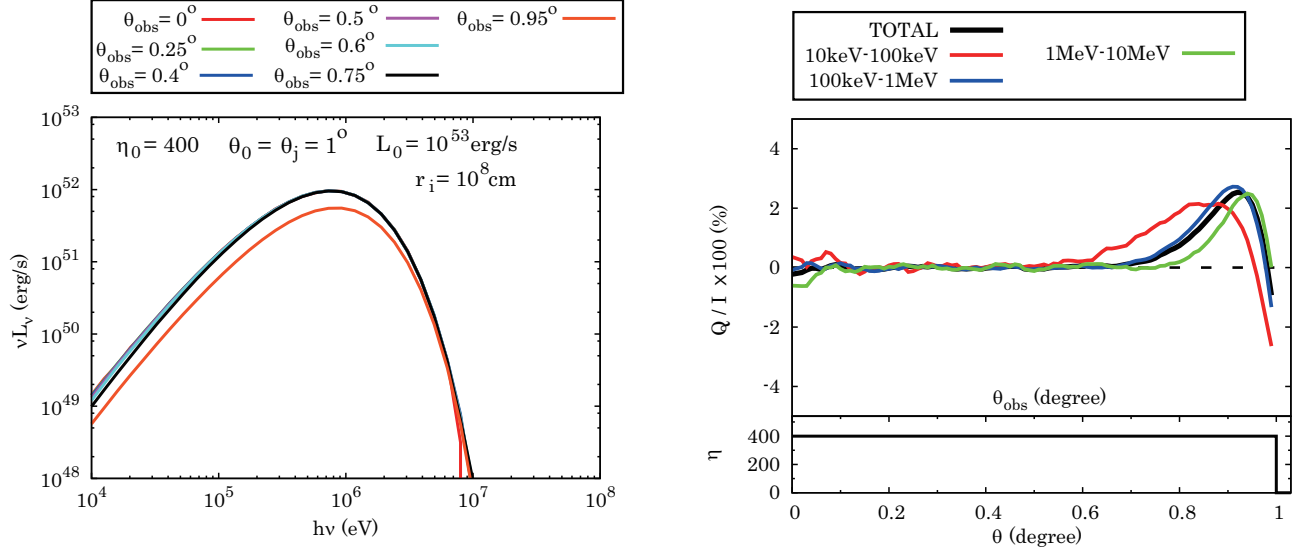


FIG. 5.— Left: Observed luminosity spectrum for a uniform jet ($\theta_0 = \theta_j = 1^\circ$) with parameters of the fireball given by $L_0 = 10^{53} \text{ erg s}^{-1}$, $\eta_0 = 400$ and $r_i = 10^8 \text{ cm}$. The various solid lines correspond to the different observer angles as shown in the legend. Right: Polarization degree (top) and dimensionless entropy (bottom) as a functions of observer angle and lateral position of jet, respectively. The thick black solid line shows the result obtained by summing up all photons, while the solid red, blue and green lines correspond to the photons in the energy bins of 10 keV – 100 keV, 100 keV – 1 MeV and 1 MeV – 10 MeV, respectively. The dashed line indicates $Q/I = 0$ for reference. Here and in subsequent plots, we do not include the viewing angle bins that have less than 2000 photon packets to avoid low statistics. We also neglect the observers that have LOS located outside the lateral jet boundary ($\theta_{\text{obs}} > \theta_j$) as mentioned in §2.3.

spine region are identical, but those in the sheath regions are different. As for the spine region, we employ the same parameter set assumed in the uniform jet model ($\eta_0 = 400$ and $L_0 = 10^{53} \text{ erg s}^{-1}$). As for the sheath regions, we consider the cases with $\eta_1 = 200$ ($L_1 = (\eta_1/\eta_0)L_0 = 5 \times 10^{52} \text{ erg s}^{-1}$) and $\eta_1 = 100$ ($L_1 = (\eta_1/\eta_0)L_0 = 2.5 \times 10^{52} \text{ erg s}^{-1}$). In the top and bottom panels of Fig. 6, we display obtained numerical results for the former and the latter case, respectively. The left and right panels of the figure display the observed spectra and the polarization, respectively. In both cases, the initial fireball radius, half opening angle of the spine and the whole jet are fixed at $r_i = 10^8 \text{ cm}$, $\theta_0 = 0.5^\circ$ and $\theta_j = 1^\circ$, respectively.

As seen in the figure, the appearance of the spectrum deviates significantly from a thermal one. Above the thermal peak, population of photons that gained energy by crossing the boundary layer multiple times produce a non-thermal tail in the spectrum (see Paper I). The efficiency of the photon acceleration increases as the difference in the velocity (Lorentz factor) between the two regions becomes larger. Hence, the non-thermal component in the spectra is harder for larger velocity difference. The photon acceleration becomes inefficient when the photon energy becomes large enough so that the recoil of electrons cannot be neglected (Klein-Nishina effect). Hence, in all cases, the spectrum does not extend up to energies higher than $h\nu \sim \Gamma_0 m_e c^2 \sim 200(\Gamma_0/400) \text{ MeV}$. This implies that our model predicts a high energy cut-off around $\sim 100 \text{ MeV}$, when the bulk Lorentz factor of the jet is \sim a few 100.

The observed spectrum is sensitive to the observer angle. The non-thermal tail is hardest when the LOS is aligned to the boundary layer $\theta_{\text{obs}} = \theta_0 = 0.5^\circ$ and becomes softer as the deviation between θ_{obs} and θ_0 becomes larger, simply because the boundary layer corresponds to the site of photon acceleration.

The thermal peak energy and the luminosity also change with the observer angle. For an observer at $\theta_{\text{obs}} < \theta_0$, the thermal component is determined mainly by photons which have propagated through the spine region. Therefore, the peak energy and luminosity are roughly equal to the case of the uniform jet considered above in which a same set of parameters (η_0 , L_0 and r_i) is assumed.

On the other hand, for an observer at $\theta_{\text{obs}} > \theta_0$, photons which have propagated through the sheath region dominate the thermal component. Accordingly, the thermal peak energy and luminosity are roughly lower by a factor $\sim (\eta_0/\eta_1)^{8/3}(L_0/L_1)^{-5/12} = (\eta_0/\eta_1)^{27/12} \sim 4.7(\eta_{0,400}/\eta_{1,200})^{27/12}$ and $\sim (\eta_0/\eta_1)^{8/3}(L_0/L_1)^{1/3} = (\eta_0/\eta_1)^3 \sim 8(\eta_{0,400}/\eta_{1,200})^3$, respectively, where $\eta_{1,200} = \eta_1/200$. It is noted, however, that the peak luminosity can be lower by several factors when the observer angle is near the jet edge ($\theta_{\text{obs}} > \theta_j - \eta_1^{-1}$). This is due to the fact that a cone of half-opening angle $\sim \eta_1^{-1} = 0.57^\circ(\eta_{1,100})^{-1}$ around the LOS, in which most of the observable emissions are produced, exceeds the jet region, where $\eta_{1,100} = \eta_1/100$.

It is worth noting that the spectra below the thermal peaks are slightly softened, compared to those observed in the case of uniform jet $\nu L_\nu \propto \nu^2$. This is mainly due to the multi-color temperature effect.⁹ As mentioned in §3.1, at low energies, contribution of regions off-aligned from the LOS becomes significant. When the LOS of the observer lying within the spine (sheath) region the sheath (spine) region contaminates to the off-aligned region. Since each region has a different thermal peak energy, luminosity and Doppler factor, superposition of these emissions leads to a slight softening, resulting in $\nu L_\nu \propto \nu^2 \cdot \nu^{1.5}$ is observed.

⁹ Although we did not mention explicitly in the text, this effect has already been observed in the result presented in Paper I.

As seen in the right panels of Fig. 6, the polarization signal is more pronounced than the case of the uniform jet. In the case of the two-component jet, in addition to the edge of the jet, the sharp boundary layer between the spine and sheath produces another site for the break of axisymmetry around the LOS. The significant change in the emission properties around the LOS produces a prominent peak in the distribution of polarization signal for the overall emission ($h\nu = 10 \text{ keV} - 100 \text{ MeV}$: *Black lines*), at $\theta_{\text{obs}} \sim \theta_0$. The polarization degree is larger when the difference in the velocity (Lorentz factor) is larger, since the change in the emission is more prominent. In the case of $\eta_0 = 400$ and $\eta_1 = 100$, the peak polarization degree can be as high as $\sim 20\%$.

To clarify how the presence of the velocity shear and its amplitude affects the resulting polarization, we also show comparison of the assumed transverse distribution of the dimensionless entropy as well as the corresponding observed total polarization degree among the uniform jet and two-component jet models in Fig. 7.

In the case of a smaller Lorentz factor difference ($\eta_0 = 400$ and $\eta_1 = 200$), the emission is brightest near the thermal peak energies. On the other hand, in the case of larger Lorentz factor difference ($\eta_0 = 400$ and $\eta_1 = 100$), non-thermal emissions above the thermal peak energies are the brightest in most of the observer angles. Hence, the overall polarization traces the behaviour of the polarization near the thermal peak ($h\nu \sim 1 \text{ MeV}$ for $\theta_{\text{obs}} \lesssim \theta_0 = 0.5^\circ$ and $h\nu \sim 200 \text{ keV}$ for $\theta_{\text{obs}} \gtrsim \theta_0 = 0.5^\circ$) for the former case, while, in the latter case, polarization signature of the non-thermal emissions ($h\nu > 1 \text{ MeV}$ for $\theta_{\text{obs}} \lesssim \theta_0 = 0.5^\circ$ and $h\nu > 100 \text{ keV}$ for $\theta_{\text{obs}} \gtrsim \theta_0 = 0.5^\circ$) are traced.

Since the photon acceleration site is localized at a certain lateral position of the jet $\theta \sim \theta_0$, the properties of the non-thermal emission change more sensitively with lateral angle θ than the thermal emissions. Consequently, the polarization signal of the non-thermal emissions tends to be stronger than that of the thermal emissions and, therefore, overall polarization signal is stronger in the latter case than the former case. The polarization degree of the non-thermal emissions can be as high as $\sim 30 - 40\%$, when the observer is located near the edge of the jet $\theta_{\text{obs}} \sim \theta_j$ (for example, see green and magenta line in the top and bottom panels of Fig. 6, respectively).

The observer dependence of the overall polarization signal Q/I can be explained as follows: regarding the lateral θ dependence of the emitting region, the luminosity of the overall emission increases with lateral position when $\theta \leq \theta_0 = 0.5^\circ$, due to the appearance of the non-thermal photons. Hence, when the observer angle is in the range $\theta_{\text{obs}} \lesssim \theta_0 - \eta_0^{-1} \sim 0.36^\circ$, within the beaming cone around the LOS, the luminosity increases with θ . This implies that photons flux possessing negative Q is strongest within the cone. As a result, net polarization signal Q/I becomes negative. At a larger observer angle $\theta_0 - \eta_0^{-1} \sim 0.36^\circ \lesssim \theta_{\text{obs}} \lesssim \theta_0 = 0.5^\circ$, sheath region enters within the beaming cone. Since the sheath region is much dimmer than the spine region, this leads to the decrease in the photon flux with negative Q . Therefore, polarization signal Q/I increases in the positive direction as θ_{obs} increases, and reaches maximum at $\theta_{\text{obs}} \sim \theta_0$. Then, at

$\theta_{\text{obs}} \gtrsim \theta_0$, the polarization Q/I decreases rapidly with θ_{obs} and again becomes negative, since the emission region producing photon flux with positive Q decreases. This rapid decrease ceases at an observer angle below $\sim \theta_0 + \eta_0^{-1} \sim 0.64^\circ$ when the photon flux from the sheath region becomes comparable to that from the spine region. At $\theta_0 + \eta_0^{-1} \sim 0.64^\circ \lesssim \theta_{\text{obs}}$, photons from the spine region become negligible, and the observable photon flux is dominated by those emitted from the sheath region. Hence, when the total flux is dominated by the thermal photons as in the case of $\eta_0 = 400$ and $\eta_1 = 200$, overall polarization signal becomes weak since the luminosity of the emitting region is not so sensitive to the lateral position. On the other hand, when the total flux is dominated by the non-thermal photons as in the case of $\eta_0 = 400$ and $\eta_1 = 100$, the emitted photons are concentrated at the region near the boundary $\theta \sim \theta_0$, and decreases rapidly with θ . As a result, the photon flux that possesses negative Q becomes pronounced as θ_{obs} increases, which in turn leads to decrease of Q/I .

3.2.2. Non-zero boundary width $d\theta_B > 0$

Here we show the results for a two-component stratified jet model in which the boundary transition layer has a finite width ($d\theta_B > 0$). The set up of our calculation is basically the same as the case of higher velocity difference considered in the previous section (§3.2.1). In all cases, we employ the same fireball parameters ($\eta_0 = 400$, $\eta_1 = 100$, $L_0 = 10^{53} \text{ erg s}^{-1}$, $L_1 = 2.5 \times 10^{52} \text{ erg s}^{-1}$ and $r_i = 10^8 \text{ cm}$) and the midpoint of the spine-sheath boundary layer and the half-opening angle of the jet are fixed as $\theta_0 = 0.5^\circ$ and $\theta_j = 1^\circ$, respectively. The only difference is that the boundary width is finite and all the physical properties within the boundary layer is determined by linear interpolation as explained in §2.1.1.

As for the widths of the boundary layer, three cases, $d\theta_B = (5\eta_0)^{-1} \sim 0.029^\circ$, $d\theta_B = (2\eta_0)^{-1} \sim 0.072^\circ$ and $d\theta_B = \eta_0^{-1} \sim 0.14^\circ$, are considered. The numerical results are displayed in Fig. 8. While the left panels of the figure show the spectra for a given observer position, the right panels show the observer dependence of the polarization signal Q/I . Compared with the case of infinitesimal width (bottom panel of Fig. 6), while the spectra up to the thermal peak energy do not show significant difference, spectra at higher energies which are dominated by the non-thermal photons become much softer in this case. The non-thermal spectra becomes softer as the boundary layer becomes wider. This is simply because the efficiency of the photon acceleration becomes lower when the gradient of the Lorentz factor is smaller (for detail, see Paper I).

The general feature of the polarization signal does not vary from the case of spine-sheath jet having a boundary layer of infinitesimal width. Regarding the observer angle dependence, there is a characteristic peak at $\theta_{\text{obs}} \sim \theta_0 = 0.5^\circ$. As in the case shown in the previous section, polarization signal is mainly governed by the non-thermal photons that are produced at the boundary layer. The contribution of the non-thermal photons in the total emission becomes smaller as the boundary layer becomes wider. since the non-thermal photons becomes less pronounced. Therefore, the overall polarization degree ($h\nu = 10 \text{ keV} - 100 \text{ MeV}$) is lower in the cases with wider boundary widths. It should be noted,

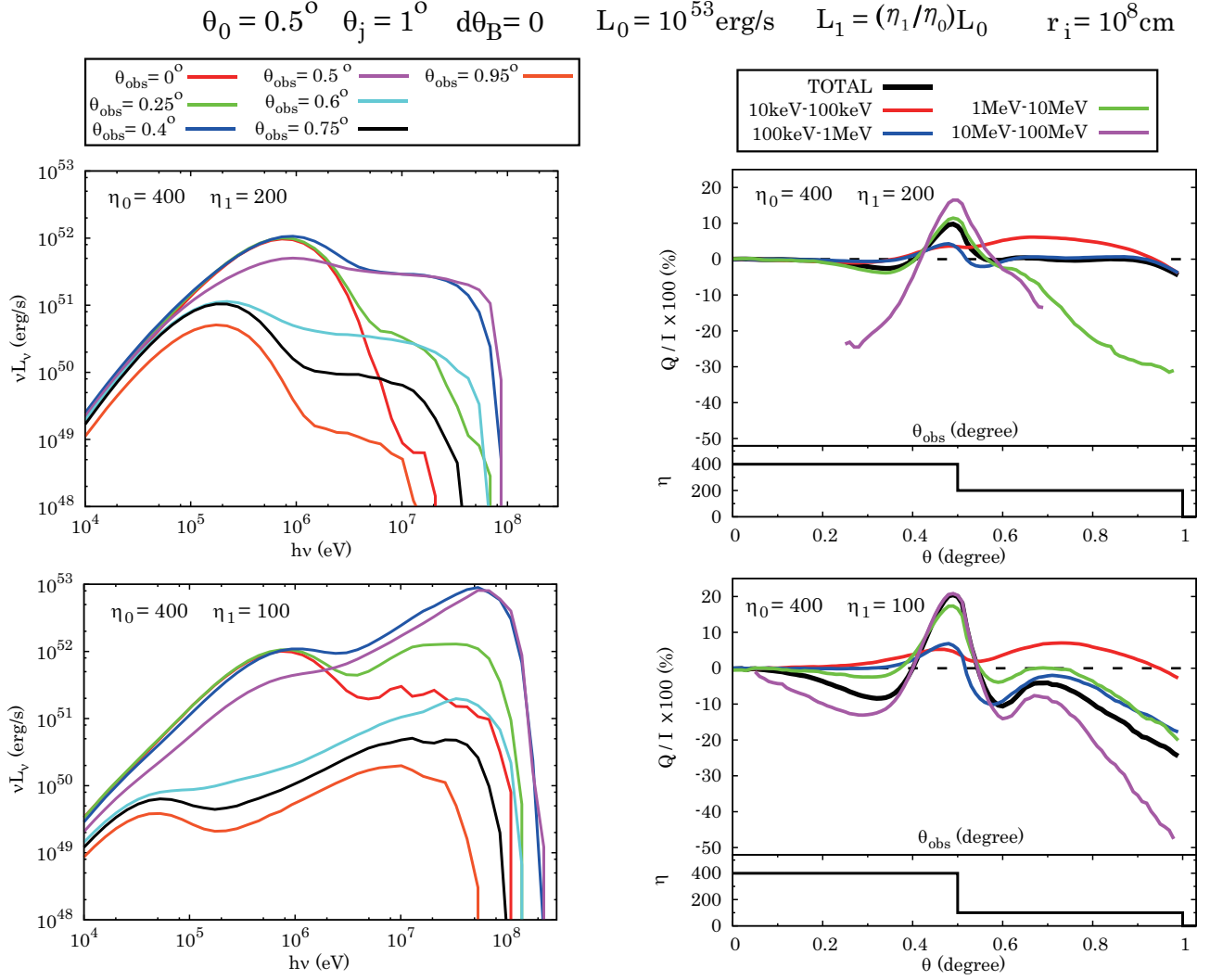


FIG. 6.— Same as Fig. 5, but for the case of a two-component (spine-sheath) jet in which the spine jet with half opening angle of $\theta_0 = 0.5^\circ$ is embedded in a wider sheath outflow with half opening angle of $\theta_j = 1^\circ$. The width of the transition boundary layer is set to be infinitesimal ($d\theta_B = 0$). The top panels show the case for sheath region with $\eta_1 = 200$ and $L_1 = (\eta_1/\eta_0)L_0 = 5 \times 10^{52} \text{ erg s}^{-1}$, while bottom panels show the case for $\eta_1 = 100$ and $L_1 = (\eta_1/\eta_0)L_0 = 2.5 \times 10^{52} \text{ erg s}^{-1}$. Fixed values are employed for dimensionless entropy (terminal Lorentz factor) and kinetic luminosity in the spine region in both cases ($\eta_0 = 400$ and $L_0 = 10^{53} \text{ erg s}^{-1}$). The initial radius of the fireball is $r_i = 10^8 \text{ cm}$ in both regions.

however, that the non-thermal photons themselves show quite high polarization degree ($\gtrsim 20\%$) even in the cases for weak non-thermal emissions (e.g., see green lines of Fig. 8).

In Fig. 9, to clarify the relation between the boundary width and the polarization signal, we show the dimensionless entropy (terminal Lorentz factor) as a function lateral position θ (bottom panel) and the overall polarization signal Q/I as a function of θ_{obs} (top panel) for the cases of $d\theta_B = 0$, $d\theta_B = (5\eta_0)^{-1}$, $d\theta_B = (2\eta_0)^{-1}$ and $d\theta_B = \eta_0^{-1}$. Indeed, it is seen that the overall polarization signal is weaker for the cases with wider boundary widths.

3.3. Multi-component Jet

Here we show the results for a stratified jet in which multiple-components are present. Let us clarify again our motivation for considering such a structure.

In the previous sections, we have shown that the emis-

sions from two-component jet that has strong velocity gradient show non-thermal spectra and accompany high polarization degree. As seen in Figs. 6 and 8, by adopting appropriate values for our parameter set, the two-component jet can reproduce the observed spectra of GRBs. For example, focusing on the case shown in the left top panel of Fig. 8 ($\eta_0 = 400$, $\eta_1 = 100$ and $d\theta_B = (5\eta_0)^{-1}$), the spectra below and above the thermal peak energy that are located at $\sim 800 \text{ keV}$ can be roughly approximated as $\nu L_\nu \propto \nu^{1.5}$ and $\nu L_\nu \propto \nu^{-0.5}$, $\nu^{-0.3}$, respectively, for an observer nearly aligned to the boundary layer $\theta_{\text{obs}} \sim 0.4 - 0.5^\circ$.

These features are consistent with the observations that are often modeled by a Band function which shows a smoothly joined broken power-law that peaks at \sim a few 100 keV. The photon indices below (α_{ph}) and above (β_{ph}) the peak energy vary from source to source ($\nu L_\nu \propto \nu^{\alpha_{\text{ph}}+2}$ for $\nu < \nu_p$ and $\nu L_\nu \propto \nu^{\beta_{\text{ph}}+2}$ for $\nu > \nu_p$), but have typical values at $\alpha_{\text{ph}} \sim -1$ and $\beta_{\text{ph}} \sim -2.5$,

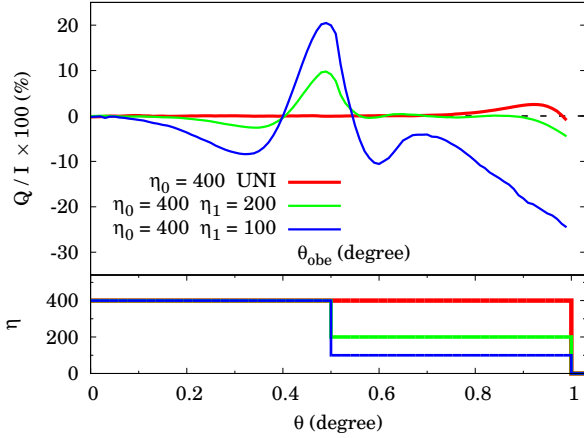


FIG. 7.— Transverse distribution of the dimensionless entropy (bottom) and total polarization degree as a function of observer angle (top) for a uniform jet ($\theta_0 = \theta_j = 1^\circ$) and a two-component jet in which the spine jet with half opening angle of $\theta_0 = 0.5^\circ$ is embedded in a wider sheath outflow with half opening angle of $\theta_j = 1^\circ$. The employed values for the dimensionless entropy (terminal Lorentz factor) and kinetic luminosity for the uniform jet and the spine region of the two-component jet are fixed as $\eta_0 = 400$ and $L_0 = 10^{53}$ erg s $^{-1}$, respectively. The initial radius of fireball is fixed as $r_i = 10^8$ cm in all cases. The red solid line shows the case of a uniform jet, while the green and blue solid lines show the cases for the two-component jet having dimensionless entropies given by $\eta_1 = 200$ and $\eta_1 = 100$ in the sheath region, respectively. In each case, the kinetic luminosity in the sheath region is given by $L_1 = (\eta_0/\eta_1)L_0$.

respectively. Hence, the high energy slope matches the typically observed value. Although the low energy slope is relatively hard, it is fairly close to the typical value ($\nu L_\nu/\nu$) and is in the range of the observation (e.g., Nava et al. 2011; Goldstein et al. 2012, 2013).

However, for an observer far off-aligned from the boundary layer, the spectra depart from the typical values. This is due to the fact that the acceleration site of the photons is located at a single fixed lateral position $\theta = \theta_0$, which suppresses the accelerated photons from spread out in various direction due to the relativistic beaming.

One possible solution to overcome this difficulty is to consider a presence of velocity shear in various lateral position of the jet. If velocity shear regions are distributed within the entire jet (closely spaced within an angular scale $\sim 2\Gamma^{-1}$), the acceleration photons will be prominent for all observers.

Indeed, large number of hydrodynamical simulations of axisymmetric jet propagation show that large velocity gradient regions, such as those accompanied by recollimation shocks, actually appear across the whole jet (Zhang et al. 2003; Mizuta et al. 2006; Morsony et al. 2007; Lazzati et al. 2009; Mizuta et al. 2011; Nagakura et al. 2011; Mizuta & Ioka 2013). Moreover, beyond the axisymmetry, we emphasize that hydrodynamical instabilities such as Rayleigh-Taylor and Richtmyer-Meshkov instabilities lead to appearance of multi-component jet having various Lorentz factor. This is shown in the recent numerical simulations by Matsumoto & Masada (2013a,b). Their results indicated that, as the jet propagate through a dense medium, these instabilities produce small scale filamentary structures that have sharp interface to distribute in entire jet re-

gions. This rich internal structure within the jet can provide acceleration site in various angular scales and remove the strong observer dependence.

Motivated by this background, we explore emissions from the jet having multiple components that have sharp velocity gradients between their interfaces. We mimic the complex structure inferred from the simulations with a simplified jet structure that has a velocity shear present at multiple lateral positions θ as described in §2. Here, we focus on the parameter ranges which result in spectra close to the typically observed ones. The obtained numerical results (spectra and polarization signal Q/I) are presented in Figs. 10-11.

In the cases shown in Fig 10, the values of the fireball parameters imposed in the C0 and C1 regions are identical to those employed in the spine and sheath regions of the two-component jet model with larger difference in the dimensionless entropy, respectively ($\eta_0 = 400$, $\eta_1 = 100$, $L_0 = 10^{53}$ erg s $^{-1}$, $L_1 = 2.5 \times 10^{52}$ erg s $^{-1}$ and $r_i = 10^8$ cm). We also impose the same value for the half-opening angle of the jet ($\theta_j = 1^\circ$). While fixed value is employed for the angular extension of C1 region ($d\theta_1 = 0.2^\circ$), from top to bottom panels, different values are employed for C0 region ($d\theta_0 = 0.3^\circ, 0.2^\circ, 0.1^\circ$ and 0.05°).

On the other hand, Fig. 11 shows the cases for a factor 2 lower values in the dimensionless entropy ($\eta_0 = 200$, $\eta_1 = 50$, $L_0 = 10^{53}$ erg s $^{-1}$, $L_1 = 2.5 \times 10^{52}$ erg s $^{-1}$ and $r_i = 10^9$ cm). The angular extensions of the jet and each components are chosen to be a factor 2 larger than the former cases (i.e., $\theta_j = 2^\circ$, $d\theta_1 = 0.4^\circ$ and $d\theta_0 = 0.6^\circ, 0.4^\circ, 0.2^\circ$ and 0.1°), since the typical spreading angle of the photons is larger by the same factor. In any case, finite values are imposed in the widths of the boundary layer ($d\theta_B = (4.5\eta_0)^{-1}$, $(4\eta_0)^{-1}$ or $(3.5\eta_0)^{-1}$).

As seen in the figures, in all cases, the spectra have broad non-thermal shapes irrespective to the observer angle. Prominent high-energy tail is always present, since the boundary layers are located within an angle $\Gamma^{-1} \sim 0.14^\circ \Gamma_{400}^{-1}$ from the LOS of any observer, where $\Gamma_{400} = (\Gamma/400)$. The observed high energy photon indices are roughly in the range $-2.5 \lesssim \beta_{ph} \lesssim -2$. The non-thermal component shows a cut-off below $h\nu \sim \eta_0 m_e c^2 \sim 200\eta_{0,400}$ MeV, due to the Klein-Nishina effect. Hence, the spectra extends up to higher energy in the cases for high dimensionless entropies $\eta_0 = 400$ (Fig. 10) than those for low dimensionless entropies (Fig. 11).

Since the photon flux from the C0 regions largely exceeds those from the C1 regions at any observer angle, the peak energy is always roughly equal to the value expected from the fireball parameters of the C0 region. In the cases for the high and low dimensionless entropies, these values can be estimated as $E_p \sim 800r_{i,8}^{1/6} \eta_{0,400}^{8/3} L_{53}^{-5/12}$ keV (Fig. 10) and $E_p \sim 180r_{i,9}^{1/6} \eta_{0,200}^{8/3} L_{53}^{-5/12}$ keV (Figs. 11), respectively, where $\eta_{0,200} = \eta_0/200$ and $r_{i,9} = r_i/10^9$ cm. It is noted, however, that the effect of the photon acceleration tends to shift the peak energy to a slightly higher value when the LOS is located within the C0 region. This effect is prominent, particularly in the cases with smaller $d\theta_0$, since the fraction of photons within the C0 component that experiences the acceleration increases. On the other hand, relatively lower peak energy is found when the LOS is

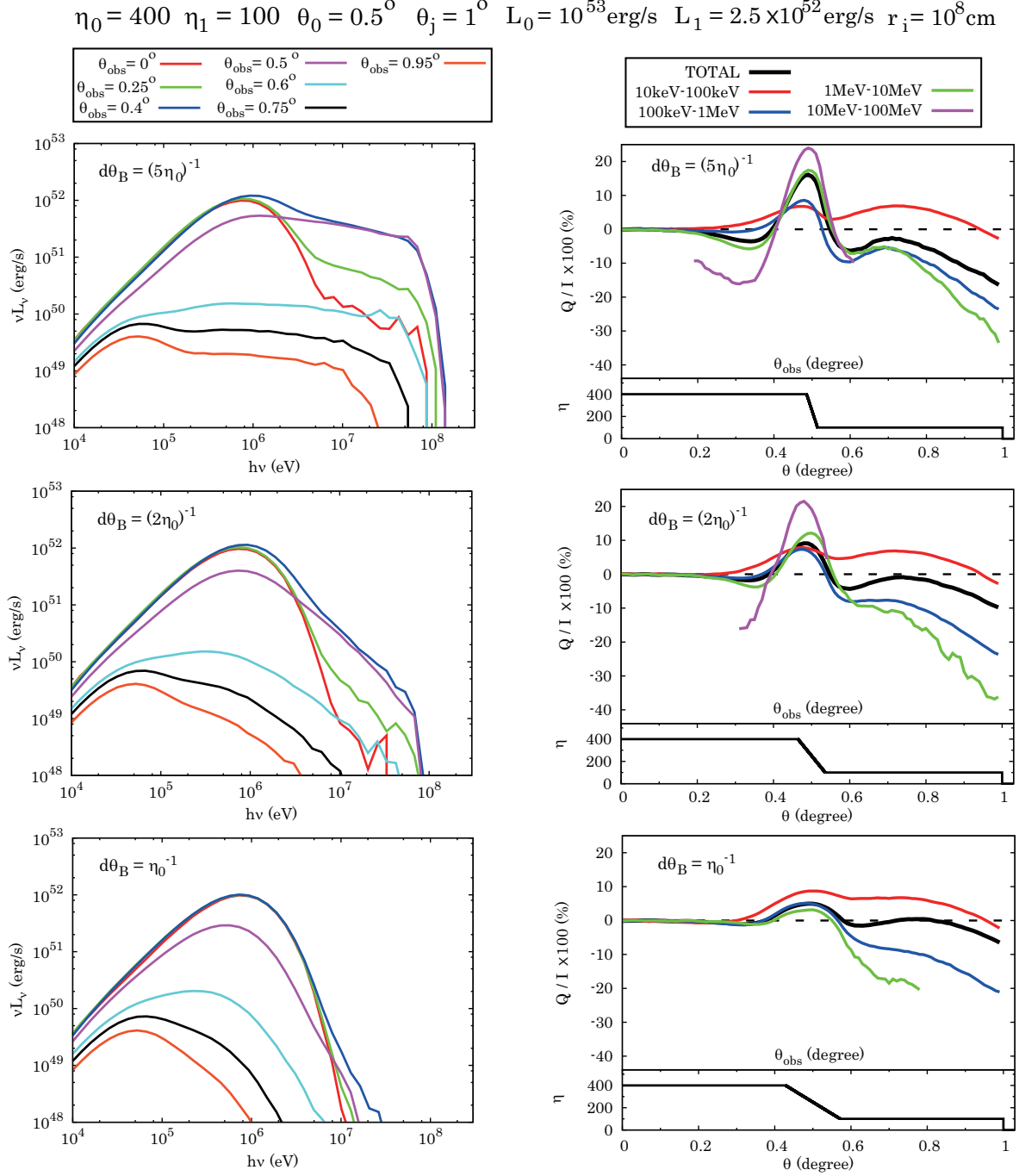


FIG. 8.— Same as bottom panels of Fig. 6, but for the cases of a finite boundary width: $d\theta_B = (5\eta_0)^{-1}$ (top), $(2\eta_0)^{-1}$ (middle) and η_0^{-1} (bottom).

within the C1 region. This is because the C0 regions are off-aligned, and, therefore, the photons emitted there have lower Doppler factors than the aligned cases.

The observed thermal peak luminosity depends on the fraction of volume occupied by C0 region within a half-opening angle $\sim \eta_0^{-1} \sim 0.14^\circ \eta_{0,400}^{-1}$ around LOS. When it is fully occupied, the peak luminosity is roughly equal to that expected from the fireball parameters of the C0 region, which are $L_p \sim 10^{52} r_{i,8}^{2/3} \eta_{0,400}^{8/3} L_{53}^{1/3} \text{ erg s}^{-1}$ (Fig. 10), and $L_p \sim 8 \times 10^{51} r_{i,9}^{2/3} \eta_{0,200}^{8/3} L_{53}^{1/3} \text{ erg s}^{-1}$ (Fig. 11) for the cases of high and low dimensionless en-

tropies, respectively. The peak luminosity decreases as the fraction of C0 component within the cone becomes smaller. Hence, although the values can vary by several factors, the observer views a brightest emission with a luminosity roughly equal to the predicted value when the LOS is located within the C0 region. Accordingly, when the width of the C0 region $d\theta_0$ is larger, the probability for the observer to see the brightest region increases. On the other hand, the luminosity drops significantly when the LOS is within the C1 region. As seen in the figures, the difference in luminosity between the two range of observer is ~ 2 orders of magnitude.

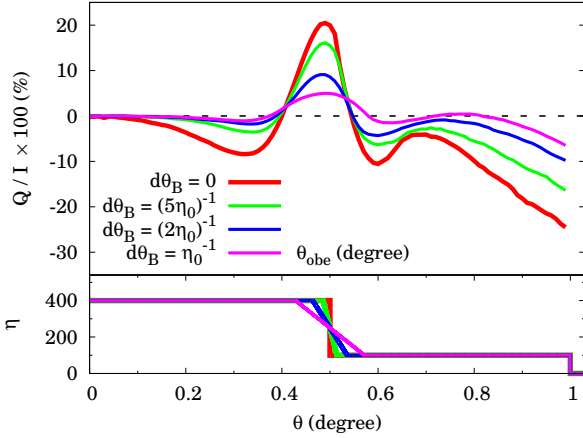


FIG. 9.— The transverse distribution of the dimensionless entropy (*bottom panel*) and total polarization degree as a function of observer angle (*top panel*) for a two-component jet model in which the spine and sheath regions are located in the transverse range $0 \leq \theta \leq \theta_0 - d\theta_B/2$ and $\theta_0 + d\theta_B/2 \leq \theta \leq \theta_j$, respectively. The figure shows the case for $\theta_0 = 0.5^\circ$ and $\theta_j = 1^\circ$. The employed values for dimensionless entropy (terminal Lorentz factor) and kinetic luminosity are chosen as $\eta_0 = 400$ and $L_0 = 10^{53}$ erg s $^{-1}$ for the spine and $\eta_1 = 100$ and $L_1 = 2.5 \times 10^{52}$ erg s $^{-1}$ for the sheath. The corresponding quantities in the boundary transition regions are determined by the linear interpolations from the two regions. The initial radius of fireball is chosen as $r_i = 10^8$ cm in all regions. The solid red, green, blue and magenta lines show the cases for the boundary layer widths of $d\theta_B = 0$, $d\theta_B = (5\eta_0)^{-1}$, $d\theta_B = (2\eta_0)^{-1}$ and $d\theta_B = \eta_0^{-1}$, respectively.

Regarding spectra below the peak, softening from the case of the uniform jet ($\alpha_{\text{ph}} \sim 0$) is seen due to the superposition of multiple components (multi-color effect) as in the case of the two-component jet. Particularly, this effect is pronounced when the LOS is located within the C1 region, since the contributions from C1 regions which enhance the emissions below the peak becomes larger. Regarding the dependence on the jet structure, the softening effect is more prominent when the width of the C0 component $d\theta_0$ is smaller, since the fraction C1 regions around the LOS tends to increase. In all cases, the observed low energy photon indices are roughly in the range $-1 \lesssim \alpha_{\text{ph}} \lesssim 0$.¹⁰

The above results show the spectral features, the high and low energy slopes (β_{ph} and α_{ph}) and peak (break) energy, that resemble typical observations. As mentioned before, this implies that typical observed spectra of GRB prompt emission can indeed be reproduced regardless of the observer angle. It is stressed that multi-component structure is favored for both the high energy and low energy spectra. To sum up, while the high energy spectra are produced by the accelerated photons at the boundary layers, the low energy spectra are produced by the superposition of thermal emissions from multiple components. We also emphasize that the existence of the cut-off at $h\nu \sim \eta_0 m_e c^2 \sim 200\eta_{0,400}$ MeV is consistent with the recent observation by LAT/*Fermi*, in the sense that these observations favor distinct emission components at energies below and above ~ 100 MeV.

As in the case of the two-component jet, large asymmetry in the emission region produced by the bound-

ary layer is the main origin of the polarization signal in the multi-component jet. Reflecting the existence of the multiple boundary layers (Fig. 3), the distribution of the polarization signal Q/I as a function of observer angle shows bumpy features (right panels of Figs. 10–11). The high energy non-thermal photons tend to have higher polarization degree $|Q|/I$, since the asymmetry is larger. The general features of the polarization do not vary largely between the cases of the high (Fig. 10) and the low dimensionless entropies (Fig. 11), but the pronounced polarization degree due to the non-thermal emissions is found at lower energies in the latter case than in the former case since thermal peak energy is lower.

The observer dependence of the overall polarization signal Q/I can be roughly understood as follows: there is no polarization signal for an on-axis observer $\theta_{\text{obs}} = 0$ in any case, since the emission region is axisymmetric around the LOS. Regarding an off-axis observer $\theta_{\text{obs}} > 0$, since the emissions originated in the C0 regions dominate over those in C1 regions at any observer angle, the distribution of C0 regions within the cone of half-opening angle $\eta_0^{-1} \sim 0.14^\circ \eta_{0,400}^{-1}$ around the LOS governs the polarization properties. When the LOS is within the C1 region, Q/I is negative in all cases, since C0 regions within the cone is localized in the edge regions that produce negative Q . When the LOS is within the C0 region, Q/I is always positive in the cases where $d\theta_0 \lesssim \eta_0^{-1}$ is satisfied (lower two panels of Figs. 10 and 11). This is due to the fact that the beaming cone is not fully occupied by C0 region but localized in the region near the LOS that produces positive Q photon flux. On the other hand, in the cases of wider C0 regions $d\theta_0 \gtrsim \eta_0^{-1}$ (upper two panels of Figs. 10 and 11), Q/I is positive when the LOS is near the boundary due to the same reason, but becomes negative near the midpoint of C0 regions. This is because the emissions near edge regions of C0 component brighter than the midpoint due to the photon acceleration effect. As a result, when the LOS is near the midpoint of C0 regions, photon flux within the beaming cone is dominated by the contribution from edge regions that emit negative Q photons.

As seen in the figures, non-negligible degree of polarization $|Q|/I \gtrsim \text{few \%}$ is present in large fraction of observer angle in all cases. These results suggest that significant polarization degree is an inherent feature of the photospheric emissions from a jet that reproduce a typical observed spectra. The polarization degree is most pronounced at high energies above the thermal peak ($h\nu \gtrsim 1$ MeV) and can be higher than $\sim 30\%$. Although relatively weak ($< 20\%$), it is emphasized that significant polarization degree $\gtrsim 10\%$ can also be found at the energy bin ($h\nu \sim 100$ keV – 1 MeV). This is particularly important, since the energy bin is relevant to the recent and future polarimeters such as GAP (70 keV – 300 keV), TSUBAME (30 keV – 200 keV) and POLAR (50 keV – 500 keV).

4. DISCUSSIONS

4.1. On the Jet Structure

In the previous section, we have shown that a broad non-thermal spectra are produced in a photospheric emission from a stratified jet. Particularly, it is demonstrated that a multi-component jet that has interfaces

¹⁰ It is worth noting that, further softening can be provided by the time evolution of the jet as shown in Paper I.

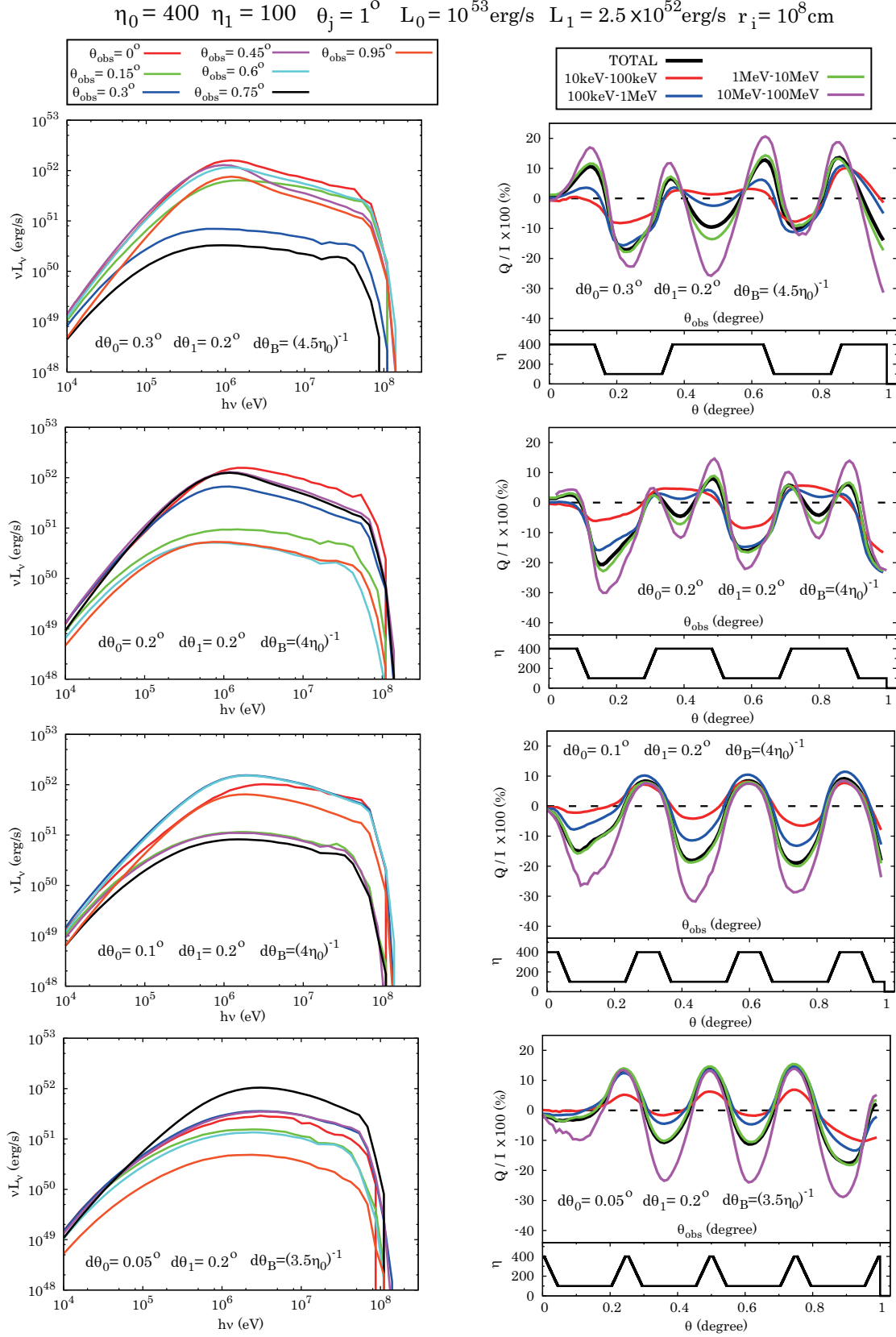


FIG. 10.— Same as Fig. 6, but for the cases of multi-component jets. Two components having fixed widths of $d\theta_0 - d\theta_B$ (C0) and $d\theta_1 - d\theta_B$ (C1) alternately appear in the transverse direction within the jet with half opening angle $\theta_j = 1^\circ$. While $d\theta_1 = 0.2^\circ$ is employed in all cases, from top to bottom panels, cases for $d\theta_0 = 0.3^\circ, 0.2^\circ, 0.1^\circ$ and 0.05° are shown. The employed values for the dimensionless entropy (terminal Lorentz factor) and kinetic luminosity are chosen as $\eta_0 = 400$ and $L_0 = 10^{53} \text{ erg s}^{-1}$ for C0 and $\eta_1 = 100$ and $L_1 = 2.5 \times 10^{52} \text{ erg s}^{-1}$ for C1 regions, respectively. The initial radius of fireball is chosen as $r_i = 10^8 \text{ cm}$ in all regions.

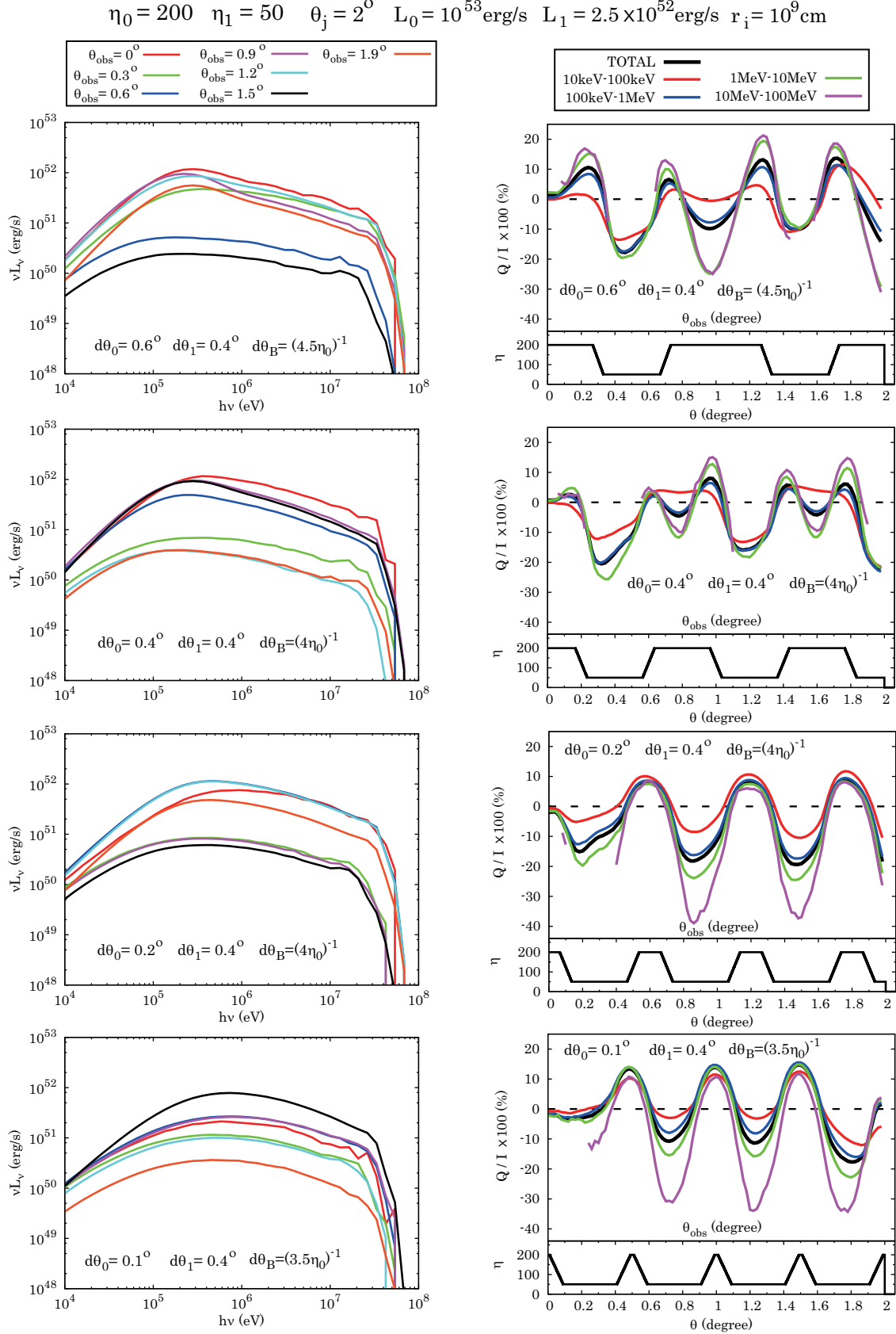


FIG. 11.— Same as Fig. 10, but for lower dimensionless entropies ($\eta_0 = 200$ and $\eta_1 = 50$), wider jet ($\theta_j = 2^\circ$) and larger initial fireball radius ($r_i = 10^9 \text{ cm}$). While $d\theta_1 = 0.4^\circ$ is employed in all cases, from top to bottom panels, case for $d\theta_0 = 0.6^\circ, 0.4^\circ, 0.2^\circ$ and 0.1° are shown.

of strong velocity gradient closely spaced within a small angular scale $\lesssim 2\Gamma^{-1}$ can reproduce the typical Band spectra irrespective to the observer angle. Although, we only explored the cases of relatively narrow jet ($\theta_j = 1^\circ$ and 2°), same results are expected for a wider jet, if similar structure develops in the entire jet.

The multi-component structure considered in the present study is motivated by the recent hydrodynamical simulations of relativistic jet which show that the velocity shear regions naturally develop within the transverse structure of the entire jet during its propagation (e.g., Matsumoto & Masada 2013a,b). Although the structure is more complex, we expect that the properties of the resulting emissions such as broad non-thermal spectra and high polarization degree are similar to the multi-component jet model. On the other hand, it is not clear whether the structure of the jet is naturally regulated to such a geometry which can reproduce the typical Band function. This is particularly important for the high energy spectra, since the photon acceleration is quite sensitive to the velocity gradient as shown in §3.2. In order to fully explore this issue, structure of the jet must be resolved in an angular scale smaller than $\sim \Gamma^{-1}$. Therefore, simulations that follow the evolution of the jets in three-dimensions with extremely high spacial resolution are required. This is beyond the scope of the present study.

4.2. Comparison with Previous Studies

In the present study, we have shown that the a significant polarization is an inherent feature of photospheric emissions from a stratified jets. Recently, Lundman et al. (2014) have performed a similar study on the photospheric emissions. The setup of their calculation is basically the same as ours, but the imposed structure in the jet is different. While we considered a multi-component jets having sharp velocity gradient in its interfaces, they considered a smoothly decaying velocity profile in lateral direction at the outer regions of the jet ($\Gamma \propto \theta^{-p}$). As in the present study, they also found that a broad non-thermal spectrum and significant polarization signal can be realized in the resulting emissions. It is noted, however, in their model, that high polarization degrees $\gtrsim 10\%$ can be detected only by an observer that has LOS aligned in the outer regions. The corresponding observed luminosities are much dimmer than that observed by an on-axis observer which views brightest emissions by an orders of magnitude. Moreover, the shapes of the spectra have strong dependence on the observer angles, and can deviate largely from the typical observations in a wide range of observer angles particularly at high energies. The main difference from their study and the most important findings of the present study are that the photospheric emissions associated in the stratified jet model can reproduce the typical observed spectra irrespective to the observer angles, and a high polarization degree $\gtrsim 10\%$ can be found not only in the observers that view dim emissions, but also those viewing brightest emissions.

Let us also consider the comparison with the synchrotron emission. The polarization properties of the synchrotron emission have been extensively studied previously (Lyutikov et al. 2003; Granot 2003; Nakar et al. 2003; Waxman 2003; Toma et al. 2009; Lazzati 2006;

Zhang & Yan 2011). In the case of the synchrotron emissions, configuration of the magnetic field as well as the structure of the jet determine the observed polarization signal. Globally ordered magnetic field configuration (e.g., helical magnetic fields around the jet axis) and wide opening angle of jet ($\theta_j \gg \Gamma^{-1}$) are favored to produce large polarization degree (Lyutikov et al. 2003; Granot 2003; Toma et al. 2009). Roughly speaking, the resulting polarization degree can be as high as $\gtrsim 40\%$ at large fraction of observer angle including those viewing the brightest emissions (Toma 2013). On the other hand, although high polarization degree up to $\sim 40\%$ can be achieved at higher frequencies, our results suggest that the polarization degree does not likely exceed $\sim 20\%$ at $h\nu \lesssim 1$ MeV (energy ranges that are relevant for polarimetry observations) in the photospheric emissions. Hence, if the detection polarization signal is confirmed at higher level ($> 20\%$), synchrotron emission is favored for the emission mechanism of GRBs. It should be noted, however, that the high polarization degree found in the synchrotron emission model is a result of the idealized assumptions such as ordered magnetic field and uniform jet structure. Disruption of magnetic field configuration and/or jet structures tend to reduce the net polarizations significantly.

4.3. Comparison with Observation of Polarization

As discussed in §4.2, observations of polarization may give crucial constraint to the emission mechanisms of GRBs. Up to now, there are only few reports for the detection of polarization but most of the results are considered to be controversial, since instrumental systematics cannot be ruled out (Coburn & Boggs 2003; Rutledge & Fox 2004; Wigger et al. 2004; Kalemci et al. 2007; McGlynn et al. 2007; Götz et al. 2009; McGlynn et al. 2009; Götz et al. 2013). Among them, the most reliable measurement is provided by the recent observations by GAP instrument on board IKAROS. In the observation, they detected quite high degree of linear polarization in the three bright GRBs which are GRB 100826A ($27 \pm 11\%$), GRB 110301A ($70 \pm 22\%$), and GRB 110721A ($84^{+16}_{-28}\%$) (Yonetoku et al. 2011, 2012). If such high polarizations ($> 20\%$) are confirmed at the high confidence level, synchrotron emission (or other optically thin emission models) may be preferred for the emission mechanism (Toma 2013) rather than the photospheric emissions as discussed above. It is noted, however, that the measurements have large uncertainty due to the lack of photon statistics and are still consistent with unpolarized photons at $\sim 3\sigma$ confidence level. Therefore, robust discussion using the polarization measurement is not possible at present. Future missions such as TSubAME (Yatsu et al. 2012) and POLAR (Orsi & Polar Collaboration 2011) may help to resolve these issues.

In addition to the indication of high degree of polarizations, GAP also reports on the time evolution in the polarization angle (the direction of electric vector of the polarized emission) in one of the observed bursts. When the observed data are split into two time intervals, a shift in the polarization angle of $\sim 90^\circ$ was found for GRB 100826A. It is worth noting that this rotation can

be explained within the framework of our model. As shown in §3.3, the polarization signal Q/I has a bumpy dependence on the observer angle and changes signs (\pm) rapidly within a small angular scale $\sim \Gamma^{-1}$. Since the positive and negative Q photons flux have polarization angle perpendicular to each other, the shift in 90° can be result from the time variability in the jet properties such as change in the width of each component and/or bends in the jet which effectively changes the observer angle (similar discussion is also given in Lundman et al. 2014).

5. SUMMARY AND CONCLUSIONS

In the present study, we have explored spectral and polarization properties of photospheric emission from ultra-relativistic jets which have a structure in the transverse direction. For the jet structure, we considered two-component and multi-component outflows that have sharp velocity shear regions between each component. The fluid properties such as electron number density $n_e(r)$ and bulk Lorentz factor $\Gamma(r)$ are determined by applying the adiabatic fireball model in each region independently. Initially, unpolarized thermal photons are injected at a radius far below the photosphere ($\tau(r_{\text{inj}} \gg 1$). Using a Monte-Carlo technique, we solve the evolution of the energy and polarization state of the injected photons via electron scatterings until they reach the outer boundary located far above the photosphere ($\tau(r_{\text{out}}) \ll 1$). Below we summarize the main results and conclusions of the present study:

1. While the majority of the injected photons escapes from the photosphere as adiabatically cooled thermal photons, small fraction of photons gains energy via Fermi-like acceleration mechanism by crossing the velocity shear regions multiple times. As a result, the accelerated photons produce a non-thermal tail above the thermal peak energy in the observed spectra. The non-thermal tail becomes harder as the velocity gradient in the shear region becomes larger due to the increase in the acceleration efficiency. Regarding the observer dependence, the non-thermal tail is most prominent when the line of sight of the observer is aligned to the velocity shear region.
2. The presence of stratified structure within the jet produces large asymmetry in the emission region around the line of sight of the observer. As a result, polarization signal is inevitably accompanied in the photospheric emission. The polarization degree tends to increase as the velocity gradient increases, since the asymmetry in the emission region is enhanced. Regarding the energy dependence, emissions at high energies tend to show higher polarization degree than those at lower energies. This

is because the emissivity of high energy (non-thermal) photons has stronger dependence on the lateral position (θ) than that of the lower energy photons, since the high energy photons produced by the photon acceleration process are concentrated near the narrow velocity shear regions.

3. Regardless of the observer angle, photospheric emission from a multi-component jet can reproduce the typical observed spectra when the velocity shear regions are spaced within an angular scale $\sim 2\Gamma^{-1}$. Prominent non-thermal tail that has photon index similar to the typical value $-2.5 \lesssim \beta_{\text{ph}} \lesssim -2$ can be present at any observer angle, since the velocity shear regions are always located within an angle $\sim \Gamma^{-1}$ from the LOS. Meanwhile, the spectrum below the peak energy is also modified from the pure thermal one, since any observer can view the thermal photons that are originated in the different components in the jet which have different peak energies. This multi-color effect leads to softening which can result in a photon indices similar to the observed ones $-1 \lesssim \alpha_{\text{ph}} \lesssim 0$. The maximum energy of the accelerated photons are limited by Klein-Nishina effect, and therefore the spectrum shows a cut-off at $\sim 200(\Gamma/400)m_e c^2$. This is also consistent with the recent observation by LAT/*Fermi*, which favor distinct emission components at energies below and above ~ 100 MeV.

4. The multi-component jet that reproduces typical observed spectra also accompanies a non-negligible polarization signal ($|Q|/I \gtrsim \text{few } \%$) in a large fraction of observer angle. The polarization degree is most pronounced at high energies above the peak energy ($h\nu \gtrsim 1$ MeV) and can be higher than $\sim 30\%$. Although relatively weak ($< 20\%$), significant polarization degree $\gtrsim 10\%$ can also be found at the energy bins ($h\nu \sim 100 - 1$ MeV) which are relevant to the recent and future polarimeters such as GAP (70 keV – 300 keV), TSUBAME (30 keV – 200 keV) and POLAR (50 keV – 500 keV).

This work is supported by the Japan Society for the Promotion of Science (No. 23340069 and No. 25610056). J.M. acknowledges support from Grants-in-Aid for Foreign JSPS Fellow (Number 24.02022). M.G.D acknowledges support from Grants-in-Aid for Foreign JSPS Fellow (Number 25.03786). S.L. acknowledges support from Grants-in-Aid for Foreign JSPS Fellow (Number 25.03018). We are grateful to Akihiro Suzuki for fruitful discussions. Numerical and data analysis were in part carried out on PC cluster at Center for Computational Astrophysics, National Astronomical Observatory of Japan.

REFERENCES

- Abdo, A. A., Ackermann, M., Ajello, M., et al. 2009, *ApJ*, 706, L138
 Abramowicz, M. A., Novikov, I. D., & Paczynski, B. 1991, *ApJ*, 369, 175
 Asano, K., & Mészáros, P. 2013, *JCAP*, 9, 8
 Band, D., Matteson, J., Ford, L., et al. 1993, *ApJ*, 413, 281
 Bai, T., & Ramaty, R. 1978, *ApJ*, 219, 705
 Bégué, D., Siutsou, I. A., & Vereshchagin, G. V. 2013, *ApJ*, 767, 139
 Beloborodov, A. M. 2010, *MNRAS*, 407, 1033
 Beloborodov, A. M. 2011, *ApJ*, 737, 68
 Chandrasekhar, S. 1960, New York: Dover, 1960,
 Coburn, W., & Boggs, S. E. 2003, *Nature*, 423, 415
 Crider, A., Liang, E. P., Smith, I. A., et al. 1997, *ApJ*, 479, L39
 Eichler, D., & Levinson, A. 2000, *ApJ*, 529, 146
 Eichler, D., & Levinson, A. 2003, *ApJ*, 596, L147
 Ghirlanda, G., Celotti, A., & Ghisellini, G. 2003, *A&A*, 406, 879
 Ghirlanda, G., Pescalli, A., & Ghisellini, G. 2013, *MNRAS*, 432, 3237
 Giannios, D. 2006, *A&A*, 457, 763
 Giannios, D. 2008, *A&A*, 480, 305
 Giannios, D., & Spruit, H. C. 2007, *A&A*, 469, 1

- Goldstein, A., Burgess, J. M., Preece, R. D., et al. 2012, *ApJS*, 199, 19
- Goldstein, A., Preece, R. D., Mallozzi, R. S., et al. 2013, *ApJS*, 208, 21
- Goodman, J. 1986, *ApJ*, 308, L47
- Götz, D., Covino, S., Fernández-Soto, A., Laurent, P., & Bošnjak, Ž. 2013, *MNRAS*, 431, 3550
- Götz, D., Laurent, P., Lebrun, F., Daigne, F., & Bošnjak, Ž. 2009, *ApJ*, 695, L208
- Granot, J. 2003, *ApJ*, 596, L17
- Guetta, D., Spada, M., & Waxman, E. 2001, *ApJ*, 557, 399
- Guiriec, S., Connaughton, V., Briggs, M. S., et al. 2011, *ApJ*, 727, L33
- Guiriec, S., Daigne, F., Hascoët, R., et al. 2013, *ApJ*, 770, 32
- Ioka, K., Murase, K., Toma, K., Nagataki, S., & Nakamura, T. 2007, *ApJ*, 670, L77
- Ito, H., Nagataki, S., Ono, M., et al. 2013, *ApJ*, 777, 62 (Paper I)
- Kalemci, E., Boggs, S. E., Kouveliotou, C., Finger, M., & Baring, M. G. 2007, *ApJS*, 169, 75
- Kaneko, Y., González, M. M., Preece, R. D., Dingus, B. L., & Briggs, M. S. 2008, *ApJ*, 677, 1168
- Kaneko, Y., Preece, R. D., Briggs, M. S., et al. 2006, *ApJS*, 166, 298
- Kino, M., Mizuta, A., & Yamada, S. 2004, *ApJ*, 611, 1021
- Kobayashi, S., Piran, T., & Sari, R. 1997, *ApJ*, 490, 92
- Lazzati, D. 2006, *New Journal of Physics*, 8, 131
- Lazzati, D., & Begelman, M. C. 2010, *ApJ*, 725, 1137
- Lazzati, D., Ghisellini, G., & Celotti, A. 1999, *MNRAS*, 309, L13
- Lazzati, D., Morsony, B. J., & Begelman, M. C. 2009, *ApJ*, 700, L47
- Lazzati, D., Morsony, B. J., Margutti, R., & Begelman, M. C. 2013, *arXiv:1301.3920*
- Lazzati, D., Rossi, E., Ghisellini, G., & Rees, M. J. 2004, *MNRAS*, 347, L1
- Levinson, A., & Eichler, D. 2004, *ApJ*, 613, 1079
- Lundman, C., Pe'er, A., & Ryde, F. 2013a, *MNRAS*, 428, 2430
- Lundman, C., Pe'er, A., & Ryde, F. 2014, *MNRAS*, 440, 3292
- Lyutikov, M., Pariev, V. I., & Blandford, R. D. 2003, *ApJ*, 597, 998
- Mao, J., & Wang, J. 2013, *ApJ*, 776, 17
- Matsumoto, J., & Masada, Y. 2013a, *ApJ*, 772, L1
- Matsumoto, J., & Masada, Y. 2013b, *European Physical Journal Web of Conferences*, 61, 2005
- McGlynn, S., Clark, D. J., Dean, A. J., et al. 2007, *A&A*, 466, 895
- McGlynn, S., Foley, S., McBreen, B., et al. 2009, *A&A*, 499, 465
- McMaster, W. H. 1961, *Reviews of Modern Physics*, 33, 8
- Mészáros, P. 2006, *Reports on Progress in Physics*, 69, 2259
- Mészáros, P., & Rees, M. J. 2000, *ApJ*, 530, 292
- Mizuta, A., & Ioka, K. 2013, *ApJ*, 777, 162
- Mizuta, A., Yamasaki, T., Nagataki, S., & Mineshige, S. 2006, *ApJ*, 651, 960
- Mizuta, A., Nagataki, S., & Aoi, J. 2011, *ApJ*, 732, 26
- Morsony, B. J., Lazzati, D., & Begelman, M. C. 2007, *ApJ*, 665, 569
- Nagakura, H., Ito, H., Kiuchi, K., & Yamada, S. 2011, *ApJ*, 731, 80
- Nakar, E., Piran, T., & Waxman, E. 2003, *JCAP*, 10, 5
- Nava, L., Ghirlanda, G., Ghisellini, G., & Celotti, A. 2011, *MNRAS*, 415, 3153
- Orsi, S., & Polar Collaboration 2011, *Astrophysics and Space Sciences Transactions*, 7, 43
- Paczynski, B. 1986, *ApJ*, 308, L43
- Pe'er, A., Mészáros, P., & Rees, M. J. 2005, *ApJ*, 635, 476
- Pe'er, A., Mészáros, P., & Rees, M. J. 2006, *ApJ*, 642, 995
- Pe'er, A., & Ryde, F. 2011, *ApJ*, 732, 49
- Pe'er, A., Zhang, B.-B., Ryde, F., et al. 2012, *MNRAS*, 420, 468
- Preece, R. D., Briggs, M. S., Mallozzi, R. S., et al. 1998, *ApJ*, 506, L23
- Preece, R. D., Briggs, M. S., Mallozzi, R. S., et al. 2000, *ApJS*, 126, 19
- Piran, T. 2004, *Reviews of Modern Physics*, 76, 1143
- Rees, M. J., & Meszaros, P. 1994, *ApJ*, 430, L93
- Rees, M. J., & Mészáros, P. 2005, *ApJ*, 628, 847
- Ruffini, R., Siutsou, I. A., & Vereshchagin, G. V. 2011, *arXiv:1110.0407*
- Rutledge, R. E., & Fox, D. B. 2004, *MNRAS*, 350, 1288
- Ryde, F., Pe'er, A., Nymark, T., et al. 2011, *MNRAS*, 415, 3693
- Ryde, F., Axelsson, M., Zhang, B. B., et al. 2010, *ApJ*, 709, L172
- Sari, R., & Piran, T. 1997, *ApJ*, 485, 270
- Shaviv, N. J., & Dar, A. 1995, *ApJ*, 447, 863
- Thompson, C. 1994, *MNRAS*, 270, 480
- Toma, K., Sakamoto, T., Zhang, B., et al. 2009, *ApJ*, 698, 1042
- Toma, K. 2013, *arXiv:1308.5733*
- Vurm, I., Beloborodov, A. M., & Poutanen, J. 2011, *ApJ*, 738, 77
- Waxman, E. 2003, *Nature*, 423, 388
- Wigger, C., Hajdas, W., Arzner, K., Güdel, M., & Zehnder, A. 2004, *ApJ*, 613, 1088
- Xu, M., Nagataki, S., Huang, Y. F., & Lee, S.-H. 2012, *ApJ*, 746, 49
- Yatsu, Y., Hayashi, M., Kawakami, K., et al. 2012, *Death of Massive Stars: Supernovae and Gamma-Ray Bursts*, 279, 423
- Yonetoku, D., Murakami, T., Gunji, S., et al. 2012, *ApJ*, 758, L1
- Yonetoku, D., Murakami, T., Gunji, S., et al. 2011, *ApJ*, 743, L30
- Yonetoku, D., Murakami, T., Gunji, S., et al. 2011, *PASJ*, 63, 625
- Zhang, W., Woosley, S. E., & MacFadyen, A. I. 2003, *ApJ*, 586, 356
- Zhang, B., & Yan, H. 2011, *ApJ*, 726, 90

APPENDIX

METHOD FOR THE CALCULATION OF POLARIZATION

Here we describe how the polarization effect is taken into account in the scattering process self-consistently in our calculation. It is noted that the method is basically identical to that used in Lundman et al. (2014). In our code, each photon packet carries four-momentum $P^\mu = (h\nu/c, h\nu/\mathbf{cn})$ (or equivalently, the frequency ν and the propagation direction \mathbf{n}) and Stokes parameters

$$S = \begin{pmatrix} I \\ Q \\ U \\ V \end{pmatrix}. \quad (\text{A1})$$

Here, the parameter I is set to be equal to the total energy carried by the corresponding photon packet. The remaining parameters are always defined in a coordinate system in which the z -axis is parallel to the photon propagation direction \mathbf{n} . We use the convention that $Q/I = 1$ ($Q/I = -1$) corresponds to a 100% linear polarization parallel to the x -axis (y -axis) of the coordinate system, $U/I = 1$ ($U/I = -1$) corresponds to a 100% linear polarization in the direction pointing at 45° from the x -axis in the anti-clockwise (clockwise) direction and $V/I = 1$ ($V/I = -1$) corresponds to a full right (left) handed circular polarization.¹¹ As mentioned in §2.2, while the global propagation of photons is

¹¹ It is noted that the parameters Q and V have opposite signs compared to those of Lundman et al. (2014) merely due to differences in their definition. Due these this differences, there are also slight changes in the formulas of the differential cross section for the scatterings and the scattering matrix shown in Eq. (A2) and (A5), respectively, from those used in their study.

computed in the laboratory frame, the scattering process which changes the four momentum and polarization state are calculated in the fluid (electron) comoving frame. Hence, in each scattering event, we first perform Lorentz transformation of the photon four-momentum and Stokes parameters from the laboratory frame to the comoving frame. Then, based on the obtained quantities in the comoving frame, the four-momentum and Stokes parameters of the scattered photons are calculated (for details of the Lorentz transformation, see, e.g., Lundman et al. 2014, and references therein). Hereafter, we focus on the description of the calculations performed in the comoving frame, and all physical quantities are evaluated in the corresponding frame.

In Fig. 12, we show the coordinate systems that are used to define the Stokes parameters of the incident and scattered photons. In each scattering event, the propagation direction of the photon after the scattering is determined based on the differential cross section of the electron scattering that depends on the polarization state of the incident photon (e.g., Bai & Ramaty 1978). While the Klein-Nishina effect is taken into account for an incident photon that has energy $h\nu_{\text{in}}$ above 100 MeV, we neglect the effect in lower energies. Hence, for a given set of Stokes parameters (defined in the $x_{\text{in}}-y_{\text{in}}$ coordinate system shown in Fig. 12), S_{in} , we employ the differential cross section given by

$$\frac{d\sigma}{d\Omega}(\theta_{\text{sc}}, \phi_{\text{sc}}) = \frac{r_0^2}{2} \left(\frac{\nu_{\text{sc}}}{\nu_{\text{in}}} \right)^2 \left[\left(\frac{\nu_{\text{in}}}{\nu_{\text{sc}}} \right)^2 + \left(\frac{\nu_{\text{sc}}}{\nu_{\text{in}}} \right)^2 - \sin^2 \theta_{\text{sc}} \left\{ 1 + \left(\frac{Q}{I} \right) \cos 2\phi_{\text{sc}} + \left(\frac{U}{I} \right) \sin 2\phi_{\text{sc}} \right\} \right], \quad (\text{A2})$$

where r_0 is the classical electron radius, and ν_{sc} is the frequency of the scattered photon determined as

$$\nu_{\text{sc}} = \begin{cases} \nu_{\text{in}} & \text{for } h\nu_{\text{in}} < 100 \text{ MeV,} \\ \nu_{\text{in}}/[1 + \nu_{\text{in}}(1 - \cos \theta_{\text{sc}})] & \text{for } h\nu_{\text{in}} \geq 100 \text{ MeV.} \end{cases} \quad (\text{A3})$$

Here, θ_{sc} and ϕ_{sc} are the angles between the propagation directions of the photon before and after scattering and between the scattering plane and the x -axis (x_{in} -axis shown in Fig. 12) of the coordinate system used to define the Stokes parameters of the incident photon, respectively. In the above equation, we assumed averaging over the isotropic electron spin distribution.

Once the scattering angles (θ_{sc} and ϕ_{sc}) are determined, we update the four-momentum of the photon by replacing it with that of the scattered photons. Then, we update the Stokes parameter by calculating the Stokes parameter of the scattered photon. In this procedure, it is convenient to employ coordinate systems that have their $x-z$ planes coinciding with the scattering plane to define the Stokes parameters for both the incident and scattered photons ($x_{\text{in,rot}}-y_{\text{in,rot}}$ and $x_{\text{sc}}-y_{\text{sc}}$ coordinate systems shown in Fig. 12 for the incident and scattered photon, respectively). Hence, we first determine the Stokes parameters of the incident photon defined in the new coordinate system ($x_{\text{in,rot}}-y_{\text{in,rot}}$ coordinate), $S_{\text{in,rot}}$, in which x -axis is pointed at an angle ϕ_{sc} in the anti-clockwise direction with respect to the original one ($x_{\text{in}}-y_{\text{in}}$ coordinate). The rotational transformation of the Stokes parameters is performed as $S_{\text{in,rot}} = L(\phi_{\text{sc}})S_{\text{in}}$, where $L(\phi_{\text{sc}})$ is the rotation matrix given by (McMaster 1961)

$$L(\phi) = \begin{pmatrix} 1 & 0 & 0 & 0 \\ 0 & \cos 2\phi & \sin 2\phi & 0 \\ 0 & -\sin 2\phi & \cos 2\phi & 0 \\ 0 & 0 & 0 & 1 \end{pmatrix}. \quad (\text{A4})$$

Using the transformed Stokes parameters, Stokes parameters after the scattering defined in the coordinate system that has $x-z$ plane coinciding with the scattering plane, S_{sc} , can be calculated by using the scattering matrix (McMaster 1961)

$$R(\theta_{\text{sc}}) = \begin{pmatrix} 1 + \cos^2 \theta_{\text{sc}} + (\nu_{\text{in}} - \nu_{\text{sc}})(1 - \cos \theta_{\text{sc}}) & -\sin^2 \theta_{\text{sc}} & 0 & 0 \\ -\sin^2 \theta_{\text{sc}} & 1 + \cos^2 \theta_{\text{sc}} & 0 & 0 \\ 0 & 0 & 2 \cos \theta_{\text{sc}} & 0 \\ 0 & 0 & 0 & 2 \cos \theta_{\text{sc}} + (\nu_{\text{in}} - \nu_{\text{sc}})(1 - \cos \theta_{\text{sc}}) \cos \theta_{\text{sc}} \end{pmatrix}, \quad (\text{A5})$$

as $S_{\text{sc}} = R(\theta_{\text{sc}})S_{\text{in,rot}}$. It is obvious from the above matrix that a photon with $V = 0$ does not obtain any circular polarization from the scattering as mentioned in §2.2. To sum up, for a given set of scattering angles and initial Stokes parameters, the Stokes parameters of the scattered photon are calculated as

$$S_{\text{sc}} = R(\theta_{\text{sc}})L(\phi_{\text{sc}})S_{\text{in}}. \quad (\text{A6})$$

Finally, we normalize the obtained Stokes parameters so that the first component I is equal to the total energy of the photon packet. Since the packet is treated as an ensemble of photons having equal frequency, the change in the total energy due to scattering is computed in the same way as its frequency (Eq. (A3)). Therefore, while the total energy of the scattered packet decreases from that of the incident packet by a factor $[1 + \nu_{\text{in}}(1 - \cos \theta_{\text{sc}})]^{-1}$ for $\nu_{\text{in}} \geq 100$ MeV, it remains constant for $\nu_{\text{in}} < 100$ MeV.

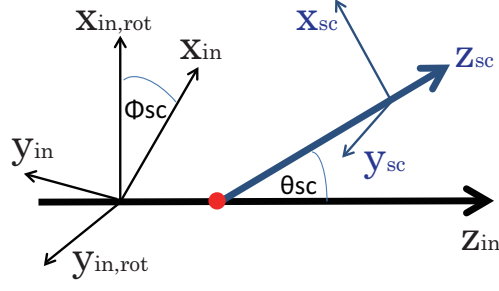


FIG. 12.— The coordinate systems that are used to calculate the scattering process in the fluid (electron) comoving frame. The z_{in} - and z_{sc} -axes are the propagation direction of the incident and scattered photon, respectively, and θ_{sc} is the angle between the two axes. The three $x - y$ coordinate systems are introduced to define the Stokes parameters of the incident and scattered photon. The initial Stokes parameters of the incident photon S_{in} is determined in the $x_{\text{in}}-y_{\text{in}}$ coordinate system. The azimuthal angle ϕ_{sc} is the angle between the scattering plane ($z_{\text{in}}-z_{\text{sc}}$ plane) and the x_{in} -axis. The $x_{\text{in,rot}}$ - and $y_{\text{in,rot}}$ -axes are defined as the coordinate system obtained by rotating the x_{in} - and y_{in} -axes around the z_{in} -axis in the anti-clockwise direction by an angle ϕ_{sc} . Hence, the $x_{\text{in,rot}}-z_{\text{in}}$ plane is aligned to the plane of scattering, and the rotated Stokes parameters of the incident photon $S_{\text{in,rot}}$ is determined in this coordinate system. The coordinate system used to define the Stokes parameters of the scattered photon S_{sc} is shown by the x_{sc} - and y_{sc} -axes. The directions of the x_{sc} - and y_{sc} -axes are determined in such a way that the $x_{\text{sc}}-z_{\text{sc}}$ plane is aligned to the plane of scattering.